

This work was written as part of one of the author's official duties as an Employee of the United States Government and is therefore a work of the United States Government. In accordance with 17 U.S.C. 105, no copyright protection is available for such works under U.S. Law.

Public Domain Mark 1.0

<https://creativecommons.org/publicdomain/mark/1.0/>

Access to this work was provided by the University of Maryland, Baltimore County (UMBC) ScholarWorks@UMBC digital repository on the Maryland Shared Open Access (MD-SOAR) platform.

Please provide feedback

Please support the ScholarWorks@UMBC repository by emailing scholarworks-group@umbc.edu and telling us what having access to this work means to you and why it's important to you. Thank you.



Numerical results for polarized light scattering in a spherical atmosphere

S. Korkin^{a,b,*}, E.-S. Yang^{b,c}, R. Spurr^d, C. Emde^{e,f}, P. Zhai^a, N. Krotkov^b, A. Vasilkov^{b,c}, A. Lyapustin^b

^a University of Maryland Baltimore County, Baltimore, MD, USA

^b NASA Goddard Space Flight Center, Greenbelt, MD, USA

^c Science Systems and Applications Inc., Lanham, MD, USA

^d RT Solutions Inc., Cambridge, MA, USA

^e Meteorological Institute, Ludwig-Maximilians-Universität, Munich, Germany

^f Deutsches Zentrum für Luft- und Raumfahrt, Oberpfaffenhofen, Germany

ARTICLE INFO

Article history:

Received 19 December 2021

Revised 1 April 2022

Accepted 4 April 2022

Available online 8 April 2022

Keywords:

Spherical atmosphere

Multiple scattering of solar light

Polarization

Validation of radiative transfer software

ABSTRACT

We report numerical results for polarized light reflection from the top of a Rayleigh scattering spherical atmosphere with height-dependent single scattering albedo over a dark surface. Michael Mishchenko considered this scenario back in the 1990's, for a plane-parallel atmosphere of unit optical thickness ($OT = 1$), for which radiance errors arising from neglecting polarization reaches their highest values. To further extend Mishchenko's results, we consider a value of $OT = 0.25$, for which the effect of atmospheric curvature is pronounced. New results are generated using three state-of-the-art radiative transfer (RT) codes. These are: the MYSTIC and MCSSA models, which simulate light scattering in a true-spherical atmosphere using Monte Carlo methods; and the discrete ordinate code VLIDORT, operating with a new multiple-scatter spherical correction designed to deliver reasonable approximations to spherical-medium scattering. In this work, we report results for both single and multiple scattering; this will help to support the validation of existing and future polarized spherical RT codes, especially those using approximative methods to deal with sphericity.

© 2022 Elsevier Ltd. All rights reserved.

1. Introduction

Recently, we published a paper reporting numerical benchmark results for Rayleigh scattering of sunlight in a spherical Earth atmosphere scenario [14]. The primary goal of that paper was to support the validation of a software that numerically simulates multiple (including single) scattering of light in a spherical planetary atmosphere - spherical radiative transfer (RT) code. The broad literature review, carried out in [14], showed that finding reliable (that is, accurate and reproducible) numerical benchmarks to test spherical RT codes was not at all straightforward. An older paper by Adams and Kattawar [1], hereinafter A&K, was found to be a rare exception. Using Monte Carlo (MC) code, A&K reported reproducible numerical results for the intensity reflected from a spherical Rayleigh scattering atmosphere of the Earth. Single and multiple scattering results were given separately, to support validation and lifetime maintenance of the RT software. Two optical thicknesses (OT), $OT = 1$ and $OT = 0.25$, were chosen to characterize physical features of the propagation of light in a spherical atmosphere. For a Rayleigh scattering atmosphere without absorption, these OTs correspond to $\lambda \approx 315$ (nm) and $\lambda \approx 435$ (nm), respectively [2]; Table 3. A&K showed that: (a) the principle of reciprocity [3]; Sec. 52, $\mu I(\mu_0, \mu, \varphi) = \mu_0 I(\mu, \mu_0, \varphi)$, does not work in a spherical atmosphere (see also A&K: p.151; here $I(\mu_0, \mu, \varphi)$ is the total intensity as a function of cosines of solar μ_0

Main Acronyms: A&K, reference to Adams and Kattawar [1]; BOA, Bottom Of Atmosphere; LOS, Line Of Sight (used only in the Appendix); MC, Monte Carlo, numerical technique; MCSSA, MC RT code for Spherical Shell Atmosphere; MS, Multiple Scattering; MSST, Multiple Scattering Source Term (used only in the Appendix); MYSTIC, Monte Carlo RT code for the physically correct tracing of photons in cloudy atmospheres; NL, Number of Layers; OT, Optical Thickness; RAZ, Relative Azimuth; RT, Radiative Transfer; SZA, Solar Zenith Angle; TOA, Top Of Atmosphere; VLIDORT, Vector Linearized Discrete Ordinate RT code; VLPS, VLIDORT Pseudo-Spherical correction; VLSC, VLIDORT MS Spherical Correction; VZA, View Zenith Angle.

* Corresponding author.

E-mail address: sergey.v.korkin@nasa.gov (S. Korkin).

Table 1

Absorption (abs), scattering (sca), and total (sum) OTs of 1km-thick layers for an atmosphere with profile $g = 1$, Eq. (1). Constant total extinction is assumed in the whole atmosphere. Each number corresponds to optical thickness between the given height, h (km), and the next level above (MYSTIC input). The top 10 and bottom 10 layers are specified here; the complete table is available in digital format from the journal website.

h, km	OT = 0.25			OT = 1		
	abs	sca	sum	abs	sca	sum
100	0.000000E+00	0.000000E+00	0.0000	0.000000E+00	0.000000E+00	0.00
99	3.121097E-06	2.496879E-03	0.0025	4.975083E-05	9.950249E-03	0.01
98	9.355498E-06	2.490645E-03	0.0025	1.487575E-04	9.851243E-03	0.01
97	1.557433E-05	2.484426E-03	0.0025	2.467790E-04	9.753221E-03	0.01
96	2.177764E-05	2.478222E-03	0.0025	3.438251E-04	9.656175E-03	0.01
95	2.796546E-05	2.472035E-03	0.0025	4.399057E-04	9.560094E-03	0.01
94	3.413782E-05	2.465862E-03	0.0025	5.350302E-04	9.464970E-03	0.01
93	4.029478E-05	2.459705E-03	0.0025	6.292082E-04	9.370792E-03	0.01
92	4.643636E-05	2.453564E-03	0.0025	7.224492E-04	9.277551E-03	0.01
91	5.256261E-05	2.447437E-03	0.0025	8.147623E-04	9.185238E-03	0.01
90	5.867356E-05	2.441326E-03	0.0025	9.061570E-04	9.093843E-03	0.01
...
10	5.012110E-04	1.998789E-03	0.0025	5.913873E-03	4.086127E-03	0.01
9	5.062017E-04	1.993798E-03	0.0025	5.954531E-03	4.045469E-03	0.01
8	5.111800E-04	1.988820E-03	0.0025	5.994784E-03	4.005216E-03	0.01
7	5.161458E-04	1.983854E-03	0.0025	6.034636E-03	3.965364E-03	0.01
6	5.210993E-04	1.978901E-03	0.0025	6.074092E-03	3.925908E-03	0.01
5	5.260403E-04	1.973960E-03	0.0025	6.113156E-03	3.886844E-03	0.01
4	5.309691E-04	1.969031E-03	0.0025	6.151830E-03	3.848170E-03	0.01
3	5.358855E-04	1.964115E-03	0.0025	6.190120E-03	3.809880E-03	0.01
2	5.407896E-04	1.959210E-03	0.0025	6.228029E-03	3.771971E-03	0.01
1	5.456816E-04	1.954318E-03	0.0025	6.265561E-03	3.734439E-03	0.01
0	5.505612E-04	1.949439E-03	0.0025	6.302719E-03	3.697281E-03	0.01
OT:			0.25			1.00

Table 2a

The solar/view geometry at TOA (MYSTIC input) as a function the geometry at BOA (VLIDORT input). For BOA, $\cos(\text{SZA}) = 0.9$, $\cos(\text{VZA})$, and RAz are shown exactly; other angles (in degrees) are rounded to two figures after the decimal point.

BOA geometry					TOA geometry		
cos(SZA)	SZA	cos(VZA)	VZA	RAz	SZA	VZA	RAz
0.9	25.84	1.0	0.00	0.00	25.84	0.00	0.00
0.9	25.84	1.0	0.00	90.00	25.84	0.00	90.00
0.9	25.84	1.0	0.00	180.00	25.84	0.00	180.00
0.9	25.84	0.9	25.84	0.00	26.27	25.41	0.00
0.9	25.84	0.9	25.84	90.00	25.85	25.41	89.12
0.9	25.84	0.9	25.84	180.00	25.41	25.41	180.00
0.9	25.84	0.8	36.87	0.00	26.50	36.21	0.00
0.9	25.84	0.8	36.87	90.00	25.85	36.21	88.64
0.9	25.84	0.8	36.87	180.00	25.18	36.21	180.00
0.9	25.84	0.7	45.57	0.00	26.74	44.68	0.00
0.9	25.84	0.7	45.57	90.00	25.86	44.68	88.15
0.9	25.84	0.7	45.57	180.00	24.95	44.68	180.00
0.9	25.84	0.6	53.13	0.00	27.01	51.97	0.00
0.9	25.84	0.6	53.13	90.00	25.87	51.97	87.60
0.9	25.84	0.6	53.13	180.00	24.68	51.97	180.00
0.9	25.84	0.5	60.00	0.00	27.34	58.50	0.00
0.9	25.84	0.5	60.00	90.00	25.88	58.50	86.91
0.9	25.84	0.5	60.00	180.00	24.34	58.50	180.00
0.9	25.84	0.4	66.42	0.00	27.79	64.47	0.00
0.9	25.84	0.4	66.42	90.00	25.91	64.47	85.98
0.9	25.84	0.4	66.42	180.00	23.89	64.47	180.00
0.9	25.84	0.3	72.54	0.00	28.47	69.92	0.00
0.9	25.84	0.3	72.54	90.00	25.97	69.92	84.60
0.9	25.84	0.3	72.54	180.00	23.22	69.92	180.00
0.9	25.84	0.2	78.46	0.00	29.58	74.72	0.00
0.9	25.84	0.2	78.46	90.00	26.09	74.72	82.33
0.9	25.84	0.2	78.46	180.00	22.10	74.72	180.00
0.9	25.84	0.1	84.26	0.00	31.69	78.41	0.00
0.9	25.84	0.1	84.26	90.00	26.45	78.41	78.11
0.9	25.84	0.1	84.26	180.00	19.99	78.41	180.00
0.9	25.84	0.05	87.13	0.00	33.46	79.52	0.00
0.9	25.84	0.05	87.13	90.00	26.87	79.52	74.70
0.9	25.84	0.05	87.13	180.00	18.23	79.52	180.00

Table 2b

Same as Table 2a, except for $\cos(\text{SZA}) = 0.1$ at BOA. Note, VLIDORT is not able to provide results for the TOA SZA exceeding 90° (see bold entries, in rows 3 and 6 from below of the table).

BOA geometry					TOA geometry		
cos(SZA)	SZA	cos(VZA)	VZA	RAz	SZA	cos(SZA)	RAz
0.1	84.26	1.0	0.00	0.00	84.26	0.00	0.00
0.1	84.26	1.0	0.00	90.00	84.26	0.00	90.00
0.1	84.26	1.0	0.00	180.00	84.26	0.00	180.00
0.1	84.26	0.9	25.84	0.00	84.69	25.41	0.00
0.1	84.26	0.9	25.84	90.00	84.26	25.41	89.96
0.1	84.26	0.9	25.84	180.00	83.83	25.41	180.00
0.1	84.26	0.8	36.87	0.00	84.92	36.21	0.00
0.1	84.26	0.8	36.87	90.00	84.26	36.21	89.93
0.1	84.26	0.8	36.87	180.00	83.60	36.21	180.00
0.1	84.26	0.7	45.57	0.00	85.16	44.68	0.00
0.1	84.26	0.7	45.57	90.00	84.26	44.68	89.91
0.1	84.26	0.7	45.57	180.00	83.36	44.68	180.00
0.1	84.26	0.6	53.13	0.00	85.43	51.97	0.00
0.1	84.26	0.6	53.13	90.00	84.26	51.97	89.88
0.1	84.26	0.6	53.13	180.00	83.10	51.97	180.00
0.1	84.26	0.5	60.00	0.00	85.76	58.50	0.00
0.1	84.26	0.5	60.00	90.00	84.26	58.50	89.85
0.1	84.26	0.5	60.00	180.00	82.76	58.50	180.00
0.1	84.26	0.4	66.42	0.00	86.21	64.47	0.00
0.1	84.26	0.4	66.42	90.00	84.26	64.47	89.80
0.1	84.26	0.4	66.42	180.00	82.31	64.47	180.00
0.1	84.26	0.3	72.54	0.00	86.89	69.92	0.00
0.1	84.26	0.3	72.54	90.00	84.27	69.92	89.74
0.1	84.26	0.3	72.54	180.00	81.64	69.92	180.00
0.1	84.26	0.2	78.46	0.00	88.00	74.72	0.00
0.1	84.26	0.2	78.46	90.00	84.27	74.72	89.62
0.1	84.26	0.2	78.46	180.00	80.52	74.72	180.00
0.1	84.26	0.1	84.26	0.00	90.11	78.41	0.00
0.1	84.26	0.1	84.26	90.00	84.29	78.41	89.41
0.1	84.26	0.1	84.26	180.00	78.41	78.41	180.00
0.1	84.26	0.05	87.13	0.00	91.88	79.52	0.00
0.1	84.26	0.05	87.13	90.00	84.31	79.52	89.24
0.1	84.26	0.05	87.13	180.00	76.65	79.52	180.00

Table 3a

Multiple scattering results for a uniform layer, $\text{OT}=1$, $\cos(\text{SZA})=0.9$. Refer to the section entitled “Graphical and numerical results” (paragraph “Tables 3-10 contain...” and the one after) for definitions of the columns.

RAz	cos(VZA)	MYSTIC: I	MYSTIC: P	MCSSA: I	MCSSA: P	dI, %	dP, %	VLIDORT: I	VLIDORT: P	dI, %	dP, %
0	1.0	3.0163E-01	0.0770	3.0157E-01	0.0770	0.0	0.0	3.0158E-01	0.0770	0.0	0.0
0	0.9	2.6209E-01	0.3191	2.6205E-01	0.3192	0.0	0.0	2.6212E-01	0.3191	0.0	0.0
0	0.8	2.5577E-01	0.4437	2.5584E-01	0.4438	0.0	0.0	2.5583E-01	0.4437	0.0	0.0
0	0.7	2.5862E-01	0.5299	2.5862E-01	0.5299	0.0	0.0	2.5869E-01	0.5297	0.0	0.0
0	0.6	2.6850E-01	0.5828	2.6851E-01	0.5828	0.0	0.0	2.6858E-01	0.5825	0.0	0.0
0	0.5	2.8469E-01	0.6055	2.8467E-01	0.6058	0.0	0.0	2.8477E-01	0.6054	0.0	0.0
0	0.4	3.0642E-01	0.6028	3.0640E-01	0.6027	0.0	0.0	3.0657E-01	0.6023	0.0	0.0
0	0.3	3.3230E-01	0.5790	3.3232E-01	0.5789	0.0	0.0	3.3253E-01	0.5783	0.1	-0.1
0	0.2	3.5920E-01	0.5395	3.5928E-01	0.5393	0.0	0.0	3.5957E-01	0.5386	0.1	-0.1
0	0.1	3.8299E-01	0.4862	3.8302E-01	0.4862	0.0	0.0	3.8345E-01	0.4852	0.1	-0.1
0	0.05	3.9288E-01	0.4535	3.9295E-01	0.4535	0.0	0.0	3.9344E-01	0.4525	0.1	-0.1
90	1.0	3.0161E-01	0.0770	3.0157E-01	0.0771	0.0	0.0	3.0159E-01	0.0770	0.0	0.0
90	0.9	3.0269E-01	0.1668	3.0267E-01	0.1667	0.0	0.0	3.0267E-01	0.1667	0.0	0.0
90	0.8	3.0544E-01	0.2441	3.0551E-01	0.2443	0.0	0.0	3.0553E-01	0.2442	0.0	0.0
90	0.7	3.1035E-01	0.3176	3.1036E-01	0.3178	0.0	0.0	3.1041E-01	0.3177	0.0	0.0
90	0.6	3.1735E-01	0.3878	3.1738E-01	0.3878	0.0	0.0	3.1745E-01	0.3876	0.0	0.0
90	0.5	3.2654E-01	0.4534	3.2652E-01	0.4534	0.0	0.0	3.2666E-01	0.4532	0.0	0.0
90	0.4	3.3728E-01	0.5133	3.3736E-01	0.5134	0.0	0.0	3.3758E-01	0.5131	0.1	0.0
90	0.3	3.4863E-01	0.5665	3.4858E-01	0.5664	0.0	0.0	3.4892E-01	0.5661	0.1	0.0
90	0.2	3.5778E-01	0.6115	3.5768E-01	0.6116	0.0	0.0	3.5805E-01	0.6111	0.1	0.0
90	0.1	3.6156E-01	0.6458	3.6168E-01	0.6457	0.0	0.0	3.6212E-01	0.6450	0.2	-0.1
90	0.05	3.6194E-01	0.6554	3.6192E-01	0.6556	0.0	0.0	3.6242E-01	0.6548	0.1	-0.1
180	1.0	3.0157E-01	0.0769	3.0157E-01	0.0770	0.0	0.0	3.0159E-01	0.0770	0.0	0.0
180	0.9	3.5267E-01	0.0182	3.5272E-01	0.0181	0.0	0.0	3.5271E-01	0.0182	0.0	0.0
180	0.8	3.7444E-01	0.0114	3.7454E-01	0.0113	0.0	0.0	3.7449E-01	0.0114	0.0	0.0
180	0.7	3.9141E-01	0.0142	3.9139E-01	0.0145	0.0	0.0	3.9142E-01	0.0142	0.0	0.0
180	0.6	4.0581E-01	0.0517	4.0583E-01	0.0516	0.0	0.0	4.0593E-01	0.0515	0.0	0.0
180	0.5	4.1851E-01	0.0981	4.1849E-01	0.0982	0.0	0.0	4.1865E-01	0.0980	0.0	0.0
180	0.4	4.2902E-01	0.1531	4.2903E-01	0.1530	0.0	0.0	4.2919E-01	0.1528	0.0	0.0
180	0.3	4.3564E-01	0.2161	4.3570E-01	0.2161	0.0	0.0	4.3593E-01	0.2157	0.1	0.0
180	0.2	4.3541E-01	0.2877	4.3543E-01	0.2877	0.0	0.0	4.3578E-01	0.2873	0.1	0.0
180	0.1	4.2525E-01	0.3680	4.2527E-01	0.3679	0.0	0.0	4.2572E-01	0.3674	0.1	-0.1
180	0.05	4.1691E-01	0.4100	4.1696E-01	0.4097	0.0	0.0	4.1741E-01	0.4093	0.1	-0.1
MAX %						0.0	0.0				
AVR %						0.0	0.0				

Table 3b

Single scattering results for a uniform layer, OT=1, cos(SZA)=0.9.

RAZ	cos(VZA)	MYSTIC: I	MYSTIC: P	MCSSA: I	MCSSA: P	dI, %	dP, %	VLIDORT: I	VLIDORT: P	dI, %	dP, %
0	1.0	1.4132E-01	0.1050	1.4134E-01	0.1050	0.0	0.0	1.4134E-01	0.1050	0.0	0.0
0	0.9	1.1553E-01	0.4447	1.1551E-01	0.4447	0.0	0.0	1.1553E-01	0.4446	0.0	0.0
0	0.8	1.0837E-01	0.6526	1.0838E-01	0.6526	0.0	0.0	1.0837E-01	0.6526	0.0	0.0
0	0.7	1.0630E-01	0.8156	1.0628E-01	0.8156	0.0	0.0	1.0630E-01	0.8155	0.0	0.0
0	0.6	1.0823E-01	0.9294	1.0823E-01	0.9294	0.0	0.0	1.0823E-01	0.9294	0.0	0.0
0	0.5	1.1399E-01	0.9895	1.1399E-01	0.9895	0.0	0.0	1.1398E-01	0.9895	0.0	0.0
0	0.4	1.2363E-01	0.9969	1.2363E-01	0.9969	0.0	0.0	1.2363E-01	0.9969	0.0	0.0
0	0.3	1.3715E-01	0.9584	1.3715E-01	0.9584	0.0	0.0	1.3714E-01	0.9584	0.0	0.0
0	0.2	1.5396E-01	0.8849	1.5397E-01	0.8849	0.0	0.0	1.5395E-01	0.8850	0.0	0.0
0	0.1	1.7203E-01	0.7887	1.7202E-01	0.7887	0.0	0.0	1.7202E-01	0.7887	0.0	0.0
0	0.05	1.8012E-01	0.7356	1.8012E-01	0.7356	0.0	0.0	1.8011E-01	0.7357	0.0	0.0
90	1.0	1.4133E-01	0.1050	1.4134E-01	0.1050	0.0	0.0	1.4134E-01	0.1050	0.0	0.0
90	0.9	1.3829E-01	0.2077	1.3828E-01	0.2077	0.0	0.0	1.3828E-01	0.2076	0.0	0.0
90	0.8	1.3609E-01	0.3172	1.3610E-01	0.3172	0.0	0.0	1.3610E-01	0.3172	0.0	0.0
90	0.7	1.3497E-01	0.4317	1.3497E-01	0.4317	0.0	0.0	1.3497E-01	0.4317	0.0	0.0
90	0.6	1.3508E-01	0.5485	1.3508E-01	0.5485	0.0	0.0	1.3508E-01	0.5485	0.0	0.0
90	0.5	1.3663E-01	0.6632	1.3664E-01	0.6632	0.0	0.0	1.3663E-01	0.6632	0.0	0.0
90	0.4	1.3980E-01	0.7705	1.3981E-01	0.7705	0.0	0.0	1.3980E-01	0.7705	0.0	0.0
90	0.3	1.4457E-01	0.8641	1.4457E-01	0.8641	0.0	0.0	1.4458E-01	0.8641	0.0	0.0
90	0.2	1.5050E-01	0.9372	1.5050E-01	0.9372	0.0	0.0	1.5050E-01	0.9372	0.0	0.0
90	0.1	1.5616E-01	0.9839	1.5616E-01	0.9839	0.0	0.0	1.5615E-01	0.9839	0.0	0.0
90	0.05	1.5801E-01	0.9960	1.5802E-01	0.9960	0.0	0.0	1.5801E-01	0.9959	0.0	0.0
180	1.0	1.4134E-01	0.1050	1.4134E-01	0.1050	0.0	0.0	1.4134E-01	0.1049	0.0	0.0
180	0.9	1.6709E-01	0.0000	1.6709E-01	0.0000	0.0	0.0	1.6710E-01	0.0000	0.0	0.0
180	0.8	1.7614E-01	0.0186	1.7617E-01	0.0186	0.0	0.0	1.7616E-01	0.0186	0.0	0.0
180	0.7	1.8244E-01	0.0604	1.8246E-01	0.0604	0.0	0.0	1.8245E-01	0.0604	0.0	0.0
180	0.6	1.8748E-01	0.1174	1.8748E-01	0.1174	0.0	0.0	1.8748E-01	0.1175	0.0	0.0
180	0.5	1.9182E-01	0.1871	1.9182E-01	0.1871	0.0	0.0	1.9182E-01	0.1871	0.0	0.0
180	0.4	1.9566E-01	0.2684	1.9565E-01	0.2684	0.0	0.0	1.9566E-01	0.2684	0.0	0.0
180	0.3	1.9880E-01	0.3602	1.9880E-01	0.3602	0.0	0.0	1.9880E-01	0.3602	0.0	0.0
180	0.2	2.0038E-01	0.4614	2.0038E-01	0.4614	0.0	0.0	2.0039E-01	0.4614	0.0	0.0
180	0.1	1.9863E-01	0.5695	1.9863E-01	0.5695	0.0	0.0	1.9863E-01	0.5696	0.0	0.0
180	0.05	1.9564E-01	0.6251	1.9564E-01	0.6251	0.0	0.0	1.9564E-01	0.6250	0.0	0.0
MAX %						0.0	0.0			0.0	0.0
AVR %						0.0	0.0			0.0	0.0

Table 4a

Multiple scattering results for a layer with profile, OT=1, cos(SZA)=0.9

RAZ	cos(VZA)	MYSTIC: I	MYSTIC: P	MCSSA: I	MCSSA: P	dI, %	dP, %	VLIDORT: I	VLIDORT: P	dI, %	dP, %
0	1.0	1.6117E-01	0.0897	1.6113E-01	0.0898	0.0	0.0	1.6114E-01	0.0897	0.0	0.0
0	0.9	1.3655E-01	0.3810	1.3658E-01	0.3811	0.0	0.0	1.3659E-01	0.3810	0.0	0.0
0	0.8	1.3182E-01	0.5458	1.3179E-01	0.5458	0.0	0.0	1.3181E-01	0.5457	0.0	0.0
0	0.7	1.3273E-01	0.6671	1.3273E-01	0.6671	0.0	0.0	1.3272E-01	0.6670	0.0	0.0
0	0.6	1.3837E-01	0.7466	1.3839E-01	0.7466	0.0	0.0	1.3841E-01	0.7465	0.0	0.0
0	0.5	1.4888E-01	0.7843	1.4892E-01	0.7843	0.0	0.0	1.4893E-01	0.7842	0.0	0.0
0	0.4	1.6471E-01	0.7834	1.6471E-01	0.7834	0.0	0.0	1.6473E-01	0.7832	0.0	0.0
0	0.3	1.8624E-01	0.7498	1.8625E-01	0.7499	0.0	0.0	1.8627E-01	0.7497	0.0	0.0
0	0.2	2.1316E-01	0.6913	2.1314E-01	0.6914	0.0	0.0	2.1319E-01	0.6911	0.0	0.0
0	0.1	2.4213E-01	0.6147	2.4213E-01	0.6147	0.0	0.0	2.4222E-01	0.6144	0.0	0.0
0	0.05	2.5461E-01	0.5709	2.5461E-01	0.5708	0.0	0.0	2.5473E-01	0.5705	0.0	0.0
90	1.0	1.6115E-01	0.0896	1.6113E-01	0.0898	0.0	0.0	1.6114E-01	0.0897	0.0	0.0
90	0.9	1.6076E-01	0.1879	1.6077E-01	0.1879	0.0	0.0	1.6077E-01	0.1879	0.0	0.0
90	0.8	1.6167E-01	0.2818	1.6163E-01	0.2819	0.0	0.0	1.6164E-01	0.2818	0.0	0.0
90	0.7	1.6401E-01	0.3753	1.6403E-01	0.3753	0.0	0.0	1.6404E-01	0.3752	0.0	0.0
90	0.6	1.6829E-01	0.4670	1.6829E-01	0.4670	0.0	0.0	1.6831E-01	0.4669	0.0	0.0
90	0.5	1.7485E-01	0.5543	1.7486E-01	0.5544	0.0	0.0	1.7486E-01	0.5543	0.0	0.0
90	0.4	1.8405E-01	0.6342	1.8409E-01	0.6343	0.0	0.0	1.8412E-01	0.6341	0.0	0.0
90	0.3	1.9630E-01	0.7029	1.9629E-01	0.7029	0.0	0.0	1.9634E-01	0.7027	0.0	0.0
90	0.2	2.1084E-01	0.7568	2.1088E-01	0.7568	0.0	0.0	2.1095E-01	0.7566	0.1	0.0
90	0.1	2.2488E-01	0.7923	2.2493E-01	0.7922	0.0	0.0	2.2502E-01	0.7921	0.1	0.0
90	0.05	2.2961E-01	0.8013	2.2962E-01	0.8014	0.0	0.0	2.2973E-01	0.8011	0.1	0.0
180	1.0	1.6112E-01	0.0897	1.6113E-01	0.0898	0.0	0.0	1.6114E-01	0.0897	0.0	0.0
180	0.9	1.9084E-01	0.0104	1.9092E-01	0.0104	0.0	0.0	1.9089E-01	0.0104	0.0	0.0
180	0.8	2.0367E-01	0.0026	2.0366E-01	0.0027	0.0	0.0	2.0365E-01	0.0026	0.0	0.0
180	0.7	2.1407E-01	0.0367	2.1410E-01	0.0365	0.0	0.0	2.1410E-01	0.0365	0.0	0.0
180	0.6	2.2390E-01	0.0835	2.2393E-01	0.0836	0.0	0.0	2.2393E-01	0.0836	0.0	0.0
180	0.5	2.3394E-01	0.1413	2.3392E-01	0.1413	0.0	0.0	2.3396E-01	0.1413	0.0	0.0
180	0.4	2.4456E-01	0.2084	2.4461E-01	0.2084	0.0	0.0	2.4463E-01	0.2084	0.0	0.0
180	0.3	2.5587E-01	0.2843	2.5587E-01	0.2843	0.0	0.0	2.5591E-01	0.2842	0.0	0.0
180	0.2	2.6655E-01	0.3683	2.6650E-01	0.3683	0.0	0.0	2.6660E-01	0.3682	0.0	0.0
180	0.1	2.7264E-01	0.4596	2.7263E-01	0.4596	0.0	0.0	2.7274E-01	0.4595	0.0	0.0
180	0.05	2.7157E-01	0.5073	2.7156E-01	0.5074	0.0	0.0	2.7168E-01	0.5073	0.0	0.0
MAX %						0.0	0.0			0.1	0.0
AVR %						0.0	0.0			0.0	0.0

Table 4b

Single scattering results for a layer with profile, OT=1, cos(SZA)=0.9.

RAZ	cos(VZA)	MYSTIC: I	MYSTIC: P	MCSSA: I	MCSSA: P	dI, %	dP, %	VLIDORT: I	VLIDORT: P	dI, %	dP, %
0	1.0	1.0426E-01	0.1050	1.0424E-01	0.1050	0.0	0.0	1.0425E-01	0.1050	0.0	0.0
0	0.9	8.5760E-02	0.4447	8.5747E-02	0.4447	0.0	0.0	8.5759E-02	0.4446	0.0	0.0
0	0.8	8.1071E-02	0.6526	8.1056E-02	0.6526	0.0	0.0	8.1069E-02	0.6526	0.0	0.0
0	0.7	8.0261E-02	0.8156	8.0264E-02	0.8156	0.0	0.0	8.0266E-02	0.8155	0.0	0.0
0	0.6	8.2691E-02	0.9294	8.2679E-02	0.9294	0.0	0.0	8.2685E-02	0.9294	0.0	0.0
0	0.5	8.8384E-02	0.9895	8.8389E-02	0.9895	0.0	0.0	8.8383E-02	0.9895	0.0	0.0
0	0.4	9.7720E-02	0.9969	9.7718E-02	0.9969	0.0	0.0	9.7714E-02	0.9969	0.0	0.0
0	0.3	1.1115E-01	0.9584	1.1115E-01	0.9584	0.0	0.0	1.1113E-01	0.9584	0.0	0.0
0	0.2	1.2872E-01	0.8849	1.2872E-01	0.8849	0.0	0.0	1.2871E-01	0.8850	0.0	0.0
0	0.1	1.4860E-01	0.7887	1.4859E-01	0.7887	0.0	0.0	1.4859E-01	0.7887	0.0	0.0
0	0.05	1.5743E-01	0.7356	1.5742E-01	0.7356	0.0	0.0	1.5742E-01	0.7357	0.0	0.0
90	1.0	1.0428E-01	0.1050	1.0424E-01	0.1050	0.0	0.0	1.0425E-01	0.1050	0.0	0.0
90	0.9	1.0266E-01	0.2077	1.0265E-01	0.2077	0.0	0.0	1.0265E-01	0.2076	0.0	0.0
90	0.8	1.0180E-01	0.3172	1.0180E-01	0.3172	0.0	0.0	1.0180E-01	0.3172	0.0	0.0
90	0.7	1.0191E-01	0.4317	1.0192E-01	0.4317	0.0	0.0	1.0190E-01	0.4317	0.0	0.0
90	0.6	1.0320E-01	0.5485	1.0318E-01	0.5485	0.0	0.0	1.0318E-01	0.5485	0.0	0.0
90	0.5	1.0593E-01	0.6632	1.0594E-01	0.6632	0.0	0.0	1.0593E-01	0.6632	0.0	0.0
90	0.4	1.1048E-01	0.7705	1.1048E-01	0.7705	0.0	0.0	1.1048E-01	0.7705	0.0	0.0
90	0.3	1.1713E-01	0.8641	1.1713E-01	0.8641	0.0	0.0	1.1712E-01	0.8641	0.0	0.0
90	0.2	1.2578E-01	0.9372	1.2578E-01	0.9372	0.0	0.0	1.2577E-01	0.9372	0.0	0.0
90	0.1	1.3479E-01	0.9839	1.3480E-01	0.9839	0.0	0.0	1.3480E-01	0.9839	0.0	0.0
90	0.05	1.3799E-01	0.9960	1.3799E-01	0.9960	0.0	0.0	1.3799E-01	0.9959	0.0	0.0
180	1.0	1.0424E-01	0.1050	1.0424E-01	0.1050	0.0	0.0	1.0425E-01	0.1049	0.0	0.0
180	0.9	1.2401E-01	0.0000	1.2404E-01	0.0000	0.0	0.0	1.2403E-01	0.0000	0.0	0.0
180	0.8	1.3175E-01	0.0186	1.3175E-01	0.0186	0.0	0.0	1.3175E-01	0.0186	0.0	0.0
180	0.7	1.3776E-01	0.0604	1.3774E-01	0.0604	0.0	0.0	1.3774E-01	0.0604	0.0	0.0
180	0.6	1.4322E-01	0.1174	1.4320E-01	0.1174	0.0	0.0	1.4319E-01	0.1175	0.0	0.0
180	0.5	1.4867E-01	0.1871	1.4868E-01	0.1871	0.0	0.0	1.4869E-01	0.1871	0.0	0.0
180	0.4	1.5458E-01	0.2684	1.5459E-01	0.2684	0.0	0.0	1.5458E-01	0.2684	0.0	0.0
180	0.3	1.6100E-01	0.3602	1.6101E-01	0.3602	0.0	0.0	1.6100E-01	0.3602	0.0	0.0
180	0.2	1.6741E-01	0.4614	1.6740E-01	0.4614	0.0	0.0	1.6739E-01	0.4614	0.0	0.0
180	0.1	1.7138E-01	0.5695	1.7137E-01	0.5695	0.0	0.0	1.7137E-01	0.5696	0.0	0.0
180	0.05	1.7073E-01	0.6250	1.7073E-01	0.6251	0.0	0.0	1.7073E-01	0.6250	0.0	0.0
MAX %						0.0	0.0			0.0	0.0
AVR %						0.0	0.0			0.0	0.0

Table 5a

Multiple scattering results for a uniform layer, OT=1, cos(SZA)=0.1.

RAZ	cos(VZA)	MYSTIC: I	MYSTIC: P	MCSSA: I	MCSSA: P	dI, %	dP, %	VLIDORT: I	VLIDORT: P	dI, %	dP, %
0	1.0	4.1558E-02	0.6503	4.1544E-02	0.6506	0.0	0.0	4.1489E-02	0.6516	-0.2	0.1
0	0.9	4.7186E-02	0.5025	4.7181E-02	0.5023	0.0	0.0	4.7146E-02	0.5024	-0.1	0.0
0	0.8	5.5835E-02	0.3474	5.5843E-02	0.3473	0.0	0.0	5.5797E-02	0.3476	-0.1	0.0
0	0.7	6.5483E-02	0.2275	6.5483E-02	0.2277	0.0	0.0	6.5409E-02	0.2281	-0.1	0.1
0	0.6	7.5895E-02	0.1359	7.5856E-02	0.1361	-0.1	0.0	7.5773E-02	0.1367	-0.2	0.1
0	0.5	8.6649E-02	0.0662	8.6665E-02	0.0663	0.0	0.0	8.6547E-02	0.0670	-0.1	0.1
0	0.4	9.6933E-02	0.0137	9.6946E-02	0.0137	0.0	0.0	9.6791E-02	0.0146	-0.1	0.1
0	0.3	1.0380E-01	0.0245	1.0381E-01	0.0245	0.0	0.0	1.0364E-01	0.0235	-0.2	-0.1
0	0.2	9.7745E-02	0.0500	9.7720E-02	0.0500	0.0	0.0	9.7553E-02	0.0489	-0.2	-0.1
0	0.1	4.1894E-02	0.0750	4.1893E-02	0.0749	0.0	0.0				
0	0.05	5.6655E-03	0.1383	5.6645E-03	0.1382	0.0	0.0				
90	1.0	4.1540E-02	0.6505	4.1544E-02	0.6506	0.0	0.0	4.1489E-02	0.6516	-0.1	0.1
90	0.9	4.6431E-02	0.6691	4.6456E-02	0.6691	0.1	0.0	4.6349E-02	0.6698	-0.2	0.1
90	0.8	5.1967E-02	0.6854	5.1982E-02	0.6857	0.0	0.0	5.1860E-02	0.6861	-0.2	0.1
90	0.7	5.8311E-02	0.7006	5.8320E-02	0.7006	0.0	0.0	5.8186E-02	0.7010	-0.2	0.0
90	0.6	6.5720E-02	0.7148	6.5693E-02	0.7149	0.0	0.0	6.5561E-02	0.7153	-0.2	0.0
90	0.5	7.4424E-02	0.7294	7.4448E-02	0.7291	0.0	0.0	7.4281E-02	0.7296	-0.2	0.0
90	0.4	8.4883E-02	0.7443	8.4897E-02	0.7443	0.0	0.0	8.4734E-02	0.7448	-0.2	0.0
90	0.3	9.7493E-02	0.7610	9.7501E-02	0.7611	0.0	0.0	9.7354E-02	0.7616	-0.1	0.1
90	0.2	1.1235E-01	0.7800	1.1236E-01	0.7800	0.0	0.0	1.1225E-01	0.7806	-0.1	0.1
90	0.1	1.2752E-01	0.7989	1.2751E-01	0.7988	0.0	0.0	1.2748E-01	0.7995	0.0	0.1
90	0.05	1.3289E-01	0.8057	1.3288E-01	0.8057	0.0	0.0	1.3285E-01	0.8063	0.0	0.1
180	1.0	4.1541E-02	0.6503	4.1544E-02	0.6506	0.0	0.0	4.1489E-02	0.6515	-0.1	0.1
180	0.9	5.7060E-02	0.3598	5.7055E-02	0.3599	0.0	0.0	5.6938E-02	0.3617	-0.2	0.2
180	0.8	7.1664E-02	0.2077	7.1657E-02	0.2076	0.0	0.0	7.1511E-02	0.2092	-0.2	0.2
180	0.7	8.7896E-02	0.1053	8.7918E-02	0.1054	0.0	0.0	8.7774E-02	0.1066	-0.1	0.1
180	0.6	1.0683E-01	0.0333	1.0684E-01	0.0334	0.0	0.0	1.0670E-01	0.0343	-0.1	0.1
180	0.5	1.2963E-01	0.0178	1.2962E-01	0.0176	0.0	0.0	1.2952E-01	0.0172	-0.1	-0.1
180	0.4	1.5824E-01	0.0533	1.5826E-01	0.0533	0.0	0.0	1.5817E-01	0.0531	0.0	0.0
180	0.3	1.9584E-01	0.0764	1.9576E-01	0.0764	0.0	0.0	1.9576E-01	0.0765	0.0	0.0
180	0.2	2.4690E-01	0.0888	2.4692E-01	0.0887	0.0	0.0	2.4699E-01	0.0892	0.0	0.0
180	0.1	3.1561E-01	0.0918	3.1560E-01	0.0918	0.0	0.0	3.1585E-01	0.0925	0.1	0.1
180	0.05	3.5459E-01	0.0904	3.5460E-01	0.0904	0.0	0.0	3.5492E-01	0.0914	0.1	0.1
MAX %						0.1	0.0			0.2	0.2
AVR %						0.0	0.0			0.1	0.1

Table 5b

Single scattering results for a uniform layer, OT=1, cos(SZA)=0.1.

RAZ	cos(VZA)	MYSTIC: I	MYSTIC: P	MCSSA: I	MCSSA: P	dl, %	dP, %	VLIDORT: I	VLIDORT: P	dl, %	dP, %
0	1.0	1.9302E-02	0.9802	1.9298E-02	0.9802	0.0	0.0	1.9302E-02	0.9802	0.0	0.0
0	0.9	2.2293E-02	0.7887	2.2293E-02	0.7887	0.0	0.0	2.2297E-02	0.7887	0.0	0.0
0	0.8	2.7145E-02	0.5782	2.7141E-02	0.5782	0.0	0.0	2.7149E-02	0.5782	0.0	0.0
0	0.7	3.2750E-02	0.4181	3.2749E-02	0.4181	0.0	0.0	3.2756E-02	0.4182	0.0	0.0
0	0.6	3.9109E-02	0.2973	3.9107E-02	0.2973	0.0	0.0	3.9109E-02	0.2973	0.0	0.0
0	0.5	4.6183E-02	0.2057	4.6188E-02	0.2057	0.0	0.0	4.6188E-02	0.2057	0.0	0.0
0	0.4	5.3718E-02	0.1362	5.3710E-02	0.1362	0.0	0.0	5.3717E-02	0.1362	0.0	0.0
0	0.3	6.0359E-02	0.0841	6.0348E-02	0.0841	0.0	0.0	6.0350E-02	0.0841	0.0	0.0
0	0.2	6.0184E-02	0.0461	6.0168E-02	0.0461	0.0	0.0	6.0193E-02	0.0462	0.0	0.0
0	0.1	2.4899E-02	0.0202	2.4884E-02	0.0202	-0.1	0.0				
0	0.05	1.7202E-03	0.0113	1.7203E-03	0.0113	0.0	0.0				
90	1.0	1.9305E-02	0.9802	1.9298E-02	0.9802	0.0	0.0	1.9302E-02	0.9802	0.0	0.0
90	0.9	2.1082E-02	0.9839	2.1086E-02	0.9839	0.0	0.0	2.1082E-02	0.9839	0.0	0.0
90	0.8	2.3224E-02	0.9873	2.3235E-02	0.9873	0.0	0.0	2.3228E-02	0.9873	0.0	0.0
90	0.7	2.5857E-02	0.9902	2.5865E-02	0.9902	0.0	0.0	2.5859E-02	0.9902	0.0	0.0
90	0.6	2.9158E-02	0.9928	2.9153E-02	0.9928	0.0	0.0	2.9154E-02	0.9928	0.0	0.0
90	0.5	3.3368E-02	0.9950	3.3359E-02	0.9950	0.0	0.0	3.3367E-02	0.9950	0.0	0.0
90	0.4	3.8888E-02	0.9968	3.8885E-02	0.9968	0.0	0.0	3.8888E-02	0.9968	0.0	0.0
90	0.3	4.6270E-02	0.9982	4.6249E-02	0.9982	0.0	0.0	4.6264E-02	0.9982	0.0	0.0
90	0.2	5.6021E-02	0.9992	5.6013E-02	0.9992	0.0	0.0	5.6020E-02	0.9992	0.0	0.0
90	0.1	6.7207E-02	0.9998	6.7197E-02	0.9998	0.0	0.0	6.7212E-02	0.9998	0.0	0.0
90	0.05	7.1513E-02	1.0000	7.1500E-02	0.9999	0.0	0.0	7.1502E-02	1.0000	0.0	0.0
180	1.0	1.9295E-02	0.9802	1.9298E-02	0.9802	0.0	0.0	1.9302E-02	0.9802	0.0	0.0
180	0.9	2.7848E-02	0.5695	2.7842E-02	0.5695	0.0	0.0	2.7846E-02	0.5696	0.0	0.0
180	0.8	3.5950E-02	0.3714	3.5957E-02	0.3714	0.0	0.0	3.5960E-02	0.3714	0.0	0.0
180	0.7	4.5185E-02	0.2428	4.5176E-02	0.2428	0.0	0.0	4.5177E-02	0.2428	0.0	0.0
180	0.6	5.6146E-02	0.1543	5.6129E-02	0.1543	0.0	0.0	5.6149E-02	0.1542	0.0	0.0
180	0.5	6.9738E-02	0.0922	6.9744E-02	0.0922	0.0	0.0	6.9746E-02	0.0922	0.0	0.0
180	0.4	8.7362E-02	0.0492	8.7329E-02	0.0492	0.0	0.0	8.7343E-02	0.0492	0.0	0.0
180	0.3	1.1114E-01	0.0211	1.1114E-01	0.0211	0.0	0.0	1.1115E-01	0.0211	0.0	0.0
180	0.2	1.4422E-01	0.0051	1.4421E-01	0.0051	0.0	0.0	1.4421E-01	0.0051	0.0	0.0
180	0.1	1.8749E-01	0.0000	1.8748E-01	0.0000	0.0	0.0	1.8750E-01	0.0000	0.0	0.0
180	0.05	2.0972E-01	0.0013	2.0971E-01	0.0013	0.0	0.0	2.0971E-01	0.0013	0.0	0.0
MAX %						0.1	0.0			0.0	0.0
AVR %						0.0	0.0			0.0	0.0

Table 6a

Multiple scattering results for a layer with profile, OT=1, cos(SZA)=0.1.

RAZ	cos(VZA)	MYSTIC: I	MYSTIC: P	MCSSA: I	MCSSA: P	dl, %	dP, %	VLIDORT: I	VLIDORT: P	dl, %	dP, %
0	1.0	2.7759E-02	0.7825	2.7764E-02	0.7825	0.0	0.0	2.7764E-02	0.7827	0.0	0.0
0	0.9	3.2014E-02	0.6116	3.2019E-02	0.6115	0.0	0.0	3.2034E-02	0.6112	0.1	0.0
0	0.8	3.8659E-02	0.4308	3.8631E-02	0.4308	-0.1	0.0	3.8656E-02	0.4306	0.0	0.0
0	0.7	4.6201E-02	0.2928	4.6193E-02	0.2929	0.0	0.0	4.6211E-02	0.2928	0.0	0.0
0	0.6	5.4646E-02	0.1882	5.4650E-02	0.1883	0.0	0.0	5.4653E-02	0.1883	0.0	0.0
0	0.5	6.3874E-02	0.1086	6.3872E-02	0.1088	0.0	0.0	6.3887E-02	0.1089	0.0	0.0
0	0.4	7.3434E-02	0.0487	7.3440E-02	0.0487	0.0	0.0	7.3433E-02	0.0489	0.0	0.0
0	0.3	8.1335E-02	0.0043	8.1324E-02	0.0043	0.0	0.0	8.1335E-02	0.0046	0.0	0.0
0	0.2	7.9788E-02	0.0265	7.9776E-02	0.0266	0.0	0.0	7.9809E-02	0.0263	0.0	0.0
0	0.1	3.4361E-02	0.0520	3.4370E-02	0.0520	0.0	0.0				
0	0.05	3.5424E-03	0.0996	3.5406E-03	0.0992	-0.1	0.0				
90	1.0	2.7755E-02	0.7824	2.7764E-02	0.7824	0.0	0.0	2.7764E-02	0.7827	0.0	0.0
90	0.9	3.0994E-02	0.7930	3.1020E-02	0.7930	0.1	0.0	3.0998E-02	0.7931	0.0	0.0
90	0.8	3.4768E-02	0.8023	3.4787E-02	0.8024	0.1	0.0	3.4772E-02	0.8025	0.0	0.0
90	0.7	3.9259E-02	0.8109	3.9262E-02	0.8109	0.0	0.0	3.9247E-02	0.8110	0.0	0.0
90	0.6	4.4683E-02	0.8190	4.4673E-02	0.8189	0.0	0.0	4.4666E-02	0.8190	0.0	0.0
90	0.5	5.1371E-02	0.8268	5.1377E-02	0.8268	0.0	0.0	5.1362E-02	0.8268	0.0	0.0
90	0.4	5.9843E-02	0.8349	5.9839E-02	0.8349	0.0	0.0	5.9822E-02	0.8349	0.0	0.0
90	0.3	7.0694E-02	0.8436	7.0687E-02	0.8436	0.0	0.0	7.0692E-02	0.8436	0.0	0.0
90	0.2	8.4457E-02	0.8532	8.4468E-02	0.8531	0.0	0.0	8.4467E-02	0.8532	0.0	0.0
90	0.1	9.9570E-02	0.8627	9.9543E-02	0.8627	0.0	0.0	9.9590E-02	0.8629	0.0	0.0
90	0.05	1.0513E-01	0.8663	1.0517E-01	0.8662	0.0	0.0	1.0520E-01	0.8663	0.1	0.0
180	1.0	2.7772E-02	0.7823	2.7764E-02	0.7825	0.0	0.0	2.7764E-02	0.7827	0.0	0.0
180	0.9	3.9141E-02	0.4377	3.9132E-02	0.4377	0.0	0.0	3.9124E-02	0.4384	0.0	0.1
180	0.8	4.9988E-02	0.2643	4.9981E-02	0.2642	0.0	0.0	4.9961E-02	0.2649	-0.1	0.1
180	0.7	6.2236E-02	0.1498	6.2260E-02	0.1497	0.0	0.0	6.2219E-02	0.1504	0.0	0.1
180	0.6	7.6738E-02	0.0701	7.6742E-02	0.0701	0.0	0.0	7.6718E-02	0.0705	0.0	0.0
180	0.5	9.4520E-02	0.0138	9.4547E-02	0.0139	0.0	0.0	9.4542E-02	0.0140	0.0	0.0
180	0.4	1.1742E-01	0.0254	1.1742E-01	0.0254	0.0	0.0	1.1741E-01	0.0254	0.0	0.0
180	0.3	1.4802E-01	0.0512	1.4806E-01	0.0513	0.0	0.0	1.4807E-01	0.0513	0.0	0.0
180	0.2	1.9044E-01	0.0658	1.9048E-01	0.0658	0.0	0.0	1.9049E-01	0.0660	0.0	0.0
180	0.1	2.4654E-01	0.0702	2.4652E-01	0.0702	0.0	0.0	2.4665E-01	0.0705	0.0	0.0
180	0.05	2.7621E-01	0.0688	2.7618E-01	0.0688	0.0	0.0	2.7633E-01	0.0692	0.0	0.0
MAX %						0.1	0.0			0.1	0.1
AVR %						0.0	0.0			0.0	0.0

Table 6b

Single scattering results for a layer with profile, OT=1, cos(SZA)=0.1

RAZ	cos(VZA)	MYSTIC: I	MYSTIC: P	MCSSA: I	MCSSA: P	dI, %	dP, %	VLIDORT: I	VLIDORT: P	dI, %	dP, %
0	1.0	1.7359E-02	0.9802	1.7358E-02	0.9802	0.0	0.0	1.7357E-02	0.9802	0.0	0.0
0	0.9	2.0127E-02	0.7887	2.0128E-02	0.7887	0.0	0.0	2.0132E-02	0.7887	0.0	0.0
0	0.8	2.4581E-02	0.5782	2.4580E-02	0.5782	0.0	0.0	2.4588E-02	0.5782	0.0	0.0
0	0.7	2.9770E-02	0.4181	2.9763E-02	0.4181	0.0	0.0	2.9766E-02	0.4182	0.0	0.0
0	0.6	3.5692E-02	0.2973	3.5686E-02	0.2973	0.0	0.0	3.5683E-02	0.2973	0.0	0.0
0	0.5	4.2352E-02	0.2057	4.2350E-02	0.2057	0.0	0.0	4.2354E-02	0.2057	0.0	0.0
0	0.4	4.9583E-02	0.1362	4.9589E-02	0.1362	0.0	0.0	4.9582E-02	0.1362	0.0	0.0
0	0.3	5.6193E-02	0.0841	5.6197E-02	0.0841	0.0	0.0	5.6205E-02	0.0841	0.0	0.0
0	0.2	5.6771E-02	0.0461	5.6776E-02	0.0461	0.0	0.0	5.6796E-02	0.0462	0.0	0.0
0	0.1	2.3820E-02	0.0202	2.3828E-02	0.0202	0.0	0.0				
0	0.05	1.5964E-03	0.0113	1.5962E-03	0.0113	0.0	0.0				
90	1.0	1.7352E-02	0.9802	1.7358E-02	0.9802	0.0	0.0	1.7357E-02	0.9802	0.0	0.0
90	0.9	1.8982E-02	0.9839	1.8989E-02	0.9839	0.0	0.0	1.8983E-02	0.9839	0.0	0.0
90	0.8	2.0945E-02	0.9873	2.0946E-02	0.9873	0.0	0.0	2.0949E-02	0.9873	0.0	0.0
90	0.7	2.3366E-02	0.9902	2.3370E-02	0.9902	0.0	0.0	2.3368E-02	0.9902	0.0	0.0
90	0.6	2.6403E-02	0.9928	2.6398E-02	0.9928	0.0	0.0	2.6408E-02	0.9928	0.0	0.0
90	0.5	3.0310E-02	0.9950	3.0308E-02	0.9950	0.0	0.0	3.0318E-02	0.9950	0.0	0.0
90	0.4	3.5467E-02	0.9968	3.5473E-02	0.9968	0.0	0.0	3.5473E-02	0.9968	0.0	0.0
90	0.3	4.2418E-02	0.9982	4.2404E-02	0.9982	0.0	0.0	4.2421E-02	0.9982	0.0	0.0
90	0.2	5.1713E-02	0.9992	5.1706E-02	0.9992	0.0	0.0	5.1711E-02	0.9992	0.0	0.0
90	0.1	6.2508E-02	0.9998	6.2492E-02	0.9998	0.0	0.0	6.2511E-02	0.9998	0.0	0.0
90	0.05	6.6701E-02	1.0000	6.6696E-02	1.0000	0.0	0.0	6.6697E-02	0.9999	0.0	0.0
180	1.0	1.7352E-02	0.9802	1.7358E-02	0.9802	0.0	0.0	1.7357E-02	0.9802	0.0	0.0
180	0.9	2.4998E-02	0.5695	2.5002E-02	0.5695	0.0	0.0	2.5008E-02	0.5696	0.0	0.0
180	0.8	3.2302E-02	0.3714	3.2302E-02	0.3714	0.0	0.0	3.2303E-02	0.3714	0.0	0.0
180	0.7	4.0615E-02	0.2428	4.0618E-02	0.2428	0.0	0.0	4.0610E-02	0.2428	0.0	0.0
180	0.6	5.0542E-02	0.1543	5.0526E-02	0.1543	0.0	0.0	5.0526E-02	0.1542	0.0	0.0
180	0.5	6.2867E-02	0.0922	6.2852E-02	0.0922	0.0	0.0	6.2854E-02	0.0922	0.0	0.0
180	0.4	7.8873E-02	0.0492	7.8895E-02	0.0492	0.0	0.0	7.8874E-02	0.0492	0.0	0.0
180	0.3	1.0068E-01	0.0211	1.0065E-01	0.0211	0.0	0.0	1.0065E-01	0.0211	0.0	0.0
180	0.2	1.3105E-01	0.0051	1.3107E-01	0.0051	0.0	0.0	1.3105E-01	0.0051	0.0	0.0
180	0.1	1.7090E-01	0.0000	1.7090E-01	0.0000	0.0	0.0	1.7090E-01	0.0000	0.0	0.0
180	0.05	1.9105E-01	0.0013	1.9104E-01	0.0013	0.0	0.0	1.9104E-01	0.0013	0.0	0.0
MAX %						0.0	0.0			0.0	0.0
AVR %						0.0	0.0			0.0	0.0

Table 7a

Multiple scattering results for a uniform layer, OT=0.25, cos(SZA)=0.9.

RAZ	cos(VZA)	MYSTIC: I	MYSTIC: P	MCSSA: I	MCSSA: P	dI, %	dP, %	VLIDORT: I	VLIDORT: P	dI, %	dP, %
0	1.0	8.7804E-02	0.0940	8.7779E-02	0.0940	0.0	0.0	8.7928E-02	0.0940	0.1	0.0
0	0.9	7.4794E-02	0.4066	7.4783E-02	0.4066	0.0	0.0	7.4889E-02	0.4064	0.1	0.0
0	0.8	7.3181E-02	0.5881	7.3172E-02	0.5880	0.0	0.0	7.3282E-02	0.5877	0.1	0.0
0	0.7	7.5239E-02	0.7240	7.5242E-02	0.7240	0.0	0.0	7.5354E-02	0.7235	0.2	0.0
0	0.6	8.0838E-02	0.8143	8.0848E-02	0.8143	0.0	0.0	8.0961E-02	0.8137	0.2	-0.1
0	0.5	9.0645E-02	0.8576	9.0658E-02	0.8576	0.0	0.0	9.0800E-02	0.8569	0.2	-0.1
0	0.4	1.0618E-01	0.8566	1.0616E-01	0.8567	0.0	0.0	1.0630E-01	0.8561	0.1	0.0
0	0.3	1.2972E-01	0.8185	1.2971E-01	0.8184	0.0	0.0	1.2989E-01	0.8178	0.1	-0.1
0	0.2	1.6477E-01	0.7517	1.6476E-01	0.7517	0.0	0.0	1.6498E-01	0.7511	0.1	-0.1
0	0.1	2.1289E-01	0.6651	2.1291E-01	0.6650	0.0	0.0	2.1321E-01	0.6644	0.2	-0.1
0	0.05	2.3883E-01	0.6162	2.3882E-01	0.6163	0.0	0.0	2.3915E-01	0.6156	0.1	-0.1
90	1.0	8.7821E-02	0.0941	8.7780E-02	0.0940	0.0	0.0	8.7929E-02	0.0940	0.1	0.0
90	0.9	8.8817E-02	0.1979	8.8813E-02	0.1979	0.0	0.0	8.8954E-02	0.1979	0.2	0.0
90	0.8	9.0901E-02	0.2988	9.0884E-02	0.2988	0.0	0.0	9.1017E-02	0.2987	0.1	0.0
90	0.7	9.4331E-02	0.4001	9.4312E-02	0.4001	0.0	0.0	9.4459E-02	0.3999	0.1	0.0
90	0.6	9.9679E-02	0.5005	9.9652E-02	0.5004	0.0	0.0	9.9797E-02	0.5002	0.1	0.0
90	0.5	1.0764E-01	0.5966	1.0764E-01	0.5967	0.0	0.0	1.0780E-01	0.5964	0.1	0.0
90	0.4	1.1948E-01	0.6847	1.1948E-01	0.6848	0.0	0.0	1.1964E-01	0.6844	0.1	0.0
90	0.3	1.3694E-01	0.7604	1.3696E-01	0.7603	0.0	0.0	1.3714E-01	0.7598	0.2	-0.1
90	0.2	1.6236E-01	0.8185	1.6236E-01	0.8185	0.0	0.0	1.6259E-01	0.8180	0.1	-0.1
90	0.1	1.9582E-01	0.8551	1.9582E-01	0.8551	0.0	0.0	1.9612E-01	0.8545	0.2	-0.1
90	0.05	2.1258E-01	0.8639	2.1255E-01	0.8640	0.0	0.0	2.1287E-01	0.8634	0.1	-0.1
180	1.0	8.7836E-02	0.0941	8.7780E-02	0.0940	0.1	0.0	8.7930E-02	0.0940	0.1	0.0
180	0.9	1.0632E-01	0.0103	1.0631E-01	0.0102	0.0	0.0	1.0647E-01	0.0103	0.1	0.0
180	0.8	1.1583E-01	0.0041	1.1581E-01	0.0041	0.0	0.0	1.1597E-01	0.0040	0.1	0.0
180	0.7	1.2485E-01	0.0404	1.2480E-01	0.0403	0.0	0.0	1.2498E-01	0.0402	0.1	0.0
180	0.6	1.3464E-01	0.0905	1.3464E-01	0.0906	0.0	0.0	1.3484E-01	0.0905	0.1	0.0
180	0.5	1.4643E-01	0.1521	1.4639E-01	0.1523	0.0	0.0	1.4660E-01	0.1521	0.1	0.0
180	0.4	1.6139E-01	0.2241	1.6136E-01	0.2241	0.0	0.0	1.6158E-01	0.2239	0.1	0.0
180	0.3	1.8125E-01	0.3053	1.8126E-01	0.3053	0.0	0.0	1.8149E-01	0.3051	0.1	0.0
180	0.2	2.0787E-01	0.3949	2.0785E-01	0.3949	0.0	0.0	2.0810E-01	0.3947	0.1	0.0
180	0.1	2.3946E-01	0.4918	2.3950E-01	0.4918	0.0	0.0	2.3977E-01	0.4917	0.1	0.0
180	0.05	2.5296E-01	0.5427	2.5295E-01	0.5426	0.0	0.0	2.5325E-01	0.5425	0.1	0.0
MAX %						0.1	0.0			0.2	0.1
AVR %						0.0	0.0			0.1	0.0

Table 7b

Single scattering results for a uniform layer, OT=0.25, cos(SZA)=0.9.

RAZ	cos(VZA)	MYSTIC: I	MYSTIC: P	MCSSA: I	MCSSA: P	dI, %	dP, %	VLIDORT: I	VLIDORT: P	dI, %	dP, %
0	1.0	6.5941E-02	0.1050	6.5908E-02	0.1050	0.0	0.0	6.5934E-02	0.1050	0.0	0.0
0	0.9	5.5240E-02	0.4447	5.5227E-02	0.4447	0.0	0.0	5.5230E-02	0.4446	0.0	0.0
0	0.8	5.3350E-02	0.6526	5.3337E-02	0.6526	0.0	0.0	5.3343E-02	0.6526	0.0	0.0
0	0.7	5.4224E-02	0.8156	5.4209E-02	0.8156	0.0	0.0	5.4214E-02	0.8155	0.0	0.0
0	0.6	5.7692E-02	0.9294	5.7694E-02	0.9294	0.0	0.0	5.7692E-02	0.9294	0.0	0.0
0	0.5	6.4272E-02	0.9895	6.4261E-02	0.9895	0.0	0.0	6.4266E-02	0.9895	0.0	0.0
0	0.4	7.4949E-02	0.9969	7.4965E-02	0.9969	0.0	0.0	7.4962E-02	0.9969	0.0	0.0
0	0.3	9.1539E-02	0.9584	9.1544E-02	0.9584	0.0	0.0	9.1534E-02	0.9584	0.0	0.0
0	0.2	1.1650E-01	0.8849	1.1650E-01	0.8849	0.0	0.0	1.1648E-01	0.8850	0.0	0.0
0	0.1	1.5100E-01	0.7887	1.5100E-01	0.7887	0.0	0.0	1.5099E-01	0.7887	0.0	0.0
0	0.05	1.6958E-01	0.7356	1.6958E-01	0.7356	0.0	0.0	1.6955E-01	0.7357	0.0	0.0
90	1.0	6.5946E-02	0.1050	6.5908E-02	0.1050	-0.1	0.0	6.5935E-02	0.1050	0.0	0.0
90	0.9	6.6081E-02	0.2077	6.6064E-02	0.2077	0.0	0.0	6.6079E-02	0.2076	0.0	0.0
90	0.8	6.6954E-02	0.3172	6.6939E-02	0.3172	0.0	0.0	6.6945E-02	0.3172	0.0	0.0
90	0.7	6.8768E-02	0.4317	6.8761E-02	0.4317	0.0	0.0	6.8772E-02	0.4317	0.0	0.0
90	0.6	7.1930E-02	0.5485	7.1922E-02	0.5485	0.0	0.0	7.1918E-02	0.5485	0.0	0.0
90	0.5	7.6933E-02	0.6632	7.6922E-02	0.6632	0.0	0.0	7.6921E-02	0.6632	0.0	0.0
90	0.4	8.4609E-02	0.7705	8.4619E-02	0.7705	0.0	0.0	8.4613E-02	0.7705	0.0	0.0
90	0.3	9.6264E-02	0.8641	9.6277E-02	0.8641	0.0	0.0	9.6268E-02	0.8641	0.0	0.0
90	0.2	1.1354E-01	0.9372	1.1353E-01	0.9372	0.0	0.0	1.1351E-01	0.9372	0.0	0.0
90	0.1	1.3650E-01	0.9839	1.3650E-01	0.9839	0.0	0.0	1.3650E-01	0.9839	0.0	0.0
90	0.05	1.4802E-01	0.9960	1.4802E-01	0.9960	0.0	0.0	1.4800E-01	0.9959	0.0	0.0
180	1.0	6.5930E-02	0.1050	6.5908E-02	0.1050	0.0	0.0	6.5935E-02	0.1049	0.0	0.0
180	0.9	7.9834E-02	0.0000	7.9798E-02	0.0000	0.0	0.0	7.9812E-02	0.0000	0.0	0.0
180	0.8	8.6604E-02	0.0186	8.6577E-02	0.0186	0.0	0.0	8.6586E-02	0.0186	0.0	0.0
180	0.7	9.2894E-02	0.0604	9.2869E-02	0.0604	0.0	0.0	9.2881E-02	0.0604	0.0	0.0
180	0.6	9.9700E-02	0.1174	9.9693E-02	0.1174	0.0	0.0	9.9701E-02	0.1175	0.0	0.0
180	0.5	1.0781E-01	0.1871	1.0781E-01	0.1871	0.0	0.0	1.0783E-01	0.1871	0.0	0.0
180	0.4	1.1823E-01	0.2684	1.1820E-01	0.2684	0.0	0.0	1.1820E-01	0.2684	0.0	0.0
180	0.3	1.3208E-01	0.3602	1.3207E-01	0.3602	0.0	0.0	1.3206E-01	0.3602	0.0	0.0
180	0.2	1.5070E-01	0.4614	1.5071E-01	0.4614	0.0	0.0	1.5070E-01	0.4614	0.0	0.0
180	0.1	1.7298E-01	0.5695	1.7299E-01	0.5695	0.0	0.0	1.7297E-01	0.5696	0.0	0.0
180	0.05	1.8243E-01	0.6251	1.8245E-01	0.6251	0.0	0.0	1.8243E-01	0.6250	0.0	0.0
MAX %						0.1	0.0			0.0	0.0
AVR %						0.0	0.0			0.0	0.0

Table 8a

Multiple scattering results for a layer with profile, OT=0.25, cos(SZA)=0.9.

RAZ	cos(VZA)	MYSTIC: I	MYSTIC: P	MCSSA: I	MCSSA: P	dI, %	dP, %	VLIDORT: I	VLIDORT: P	dI, %	dP, %
0	1.0	7.5688E-02	0.0955	7.5677E-02	0.0955	0.0	0.0	7.5779E-02	0.0954	0.1	0.0
0	0.9	6.4349E-02	0.4121	6.4338E-02	0.4122	0.0	0.0	6.4407E-02	0.4119	0.1	0.0
0	0.8	6.2860E-02	0.5976	6.2863E-02	0.5975	0.0	0.0	6.2935E-02	0.5973	0.1	0.0
0	0.7	6.4593E-02	0.7375	6.4574E-02	0.7375	0.0	0.0	6.4646E-02	0.7372	0.1	0.0
0	0.6	6.9362E-02	0.8312	6.9350E-02	0.8312	0.0	0.0	6.9420E-02	0.8308	0.1	0.0
0	0.5	7.7784E-02	0.8769	7.7784E-02	0.8769	0.0	0.0	7.7874E-02	0.8765	0.1	0.0
0	0.4	9.1198E-02	0.8772	9.1188E-02	0.8772	0.0	0.0	9.1275E-02	0.8767	0.1	0.0
0	0.3	1.1166E-01	0.8389	1.1167E-01	0.8388	0.0	0.0	1.1178E-01	0.8384	0.1	-0.1
0	0.2	1.4236E-01	0.7709	1.4236E-01	0.7709	0.0	0.0	1.4248E-01	0.7705	0.1	0.0
0	0.1	1.8461E-01	0.6828	1.8467E-01	0.6827	0.0	0.0	1.8485E-01	0.6822	0.1	-0.1
0	0.05	2.0720E-01	0.6332	2.0720E-01	0.6332	0.0	0.0	2.0740E-01	0.6327	0.1	0.0
90	1.0	7.5717E-02	0.0956	7.5677E-02	0.0955	-0.1	0.0	7.5779E-02	0.0954	0.1	0.0
90	0.9	7.6516E-02	0.1994	7.6490E-02	0.1993	0.0	0.0	7.6589E-02	0.1993	0.1	0.0
90	0.8	7.8213E-02	0.3017	7.8211E-02	0.3016	0.0	0.0	7.8294E-02	0.3015	0.1	0.0
90	0.7	8.1107E-02	0.4048	8.1097E-02	0.4049	0.0	0.0	8.1191E-02	0.4048	0.1	0.0
90	0.6	8.5663E-02	0.5076	8.5637E-02	0.5076	0.0	0.0	8.5729E-02	0.5075	0.1	0.0
90	0.5	9.2485E-02	0.6066	9.2487E-02	0.6066	0.0	0.0	9.2583E-02	0.6063	0.1	0.0
90	0.4	1.0270E-01	0.6974	1.0270E-01	0.6974	0.0	0.0	1.0280E-01	0.6971	0.1	0.0
90	0.3	1.1785E-01	0.7754	1.1787E-01	0.7754	0.0	0.0	1.1799E-01	0.7751	0.1	0.0
90	0.2	1.4012E-01	0.8356	1.4009E-01	0.8356	0.0	0.0	1.4022E-01	0.8353	0.1	0.0
90	0.1	1.6943E-01	0.8735	1.6945E-01	0.8735	0.0	0.0	1.6964E-01	0.8731	0.1	0.0
90	0.05	1.8393E-01	0.8828	1.8393E-01	0.8828	0.0	0.0	1.8411E-01	0.8824	0.1	0.0
180	1.0	7.5700E-02	0.0955	7.5677E-02	0.0955	0.0	0.0	7.5780E-02	0.0954	0.1	0.0
180	0.9	9.1702E-02	0.0087	9.1684E-02	0.0088	0.0	0.0	9.1791E-02	0.0088	0.1	0.0
180	0.8	9.9906E-02	0.0062	9.9872E-02	0.0063	0.0	0.0	9.9978E-02	0.0062	0.1	0.0
180	0.7	1.0768E-01	0.0434	1.0763E-01	0.0434	0.0	0.0	1.0775E-01	0.0433	0.1	0.0
180	0.6	1.1618E-01	0.0946	1.1614E-01	0.0947	0.0	0.0	1.1626E-01	0.0946	0.1	0.0
180	0.5	1.2634E-01	0.1576	1.2632E-01	0.1577	0.0	0.0	1.2646E-01	0.1575	0.1	0.0
180	0.4	1.3938E-01	0.2309	1.3936E-01	0.2309	0.0	0.0	1.3949E-01	0.2308	0.1	0.0
180	0.3	1.5678E-01	0.3137	1.5677E-01	0.3137	0.0	0.0	1.5692E-01	0.3136	0.1	0.0
180	0.2	1.8025E-01	0.4051	1.8022E-01	0.4051	0.0	0.0	1.8037E-01	0.4050	0.1	0.0
180	0.1	2.0818E-01	0.5037	2.0822E-01	0.5037	0.0	0.0	2.0838E-01	0.5037	0.1	0.0
180	0.05	2.1988E-01	0.5553	2.1986E-01	0.5553	0.0	0.0	2.2004E-01	0.5553	0.1	0.0
MAX %						0.1	0.0			0.1	0.1
AVR %						0.0	0.0			0.1	0.0

Table 8b

Single scattering results for a layer with profile, OT=0.25, cos(SZA)=0.9

RAZ	cos(VZA)	MYSTIC: I	MYSTIC: P	MCSSA: I	MCSSA: P	dI, %	dP, %	VLIDORT: I	VLIDORT: P	dI, %	dP, %
0	1.0	5.8983E-02	0.1050	5.8955E-02	0.1050	0.0	0.0	5.8977E-02	0.1050	0.0	0.0
0	0.9	4.9432E-02	0.4447	4.9422E-02	0.4447	0.0	0.0	4.9426E-02	0.4446	0.0	0.0
0	0.8	4.7779E-02	0.6526	4.7759E-02	0.6526	0.0	0.0	4.7766E-02	0.6526	0.0	0.0
0	0.7	4.8588E-02	0.8156	4.8575E-02	0.8156	0.0	0.0	4.8581E-02	0.8155	0.0	0.0
0	0.6	5.1734E-02	0.9294	5.1746E-02	0.9294	0.0	0.0	5.1746E-02	0.9294	0.0	0.0
0	0.5	5.7705E-02	0.9895	5.7707E-02	0.9895	0.0	0.0	5.7711E-02	0.9895	0.0	0.0
0	0.4	6.7435E-02	0.9969	6.7430E-02	0.9969	0.0	0.0	6.7427E-02	0.9969	0.0	0.0
0	0.3	8.2524E-02	0.9584	8.2528E-02	0.9584	0.0	0.0	8.2519E-02	0.9584	0.0	0.0
0	0.2	1.0536E-01	0.8849	1.0535E-01	0.8849	0.0	0.0	1.0533E-01	0.8850	0.0	0.0
0	0.1	1.3697E-01	0.7887	1.3698E-01	0.7887	0.0	0.0	1.3697E-01	0.7887	0.0	0.0
0	0.05	1.5385E-01	0.7356	1.5384E-01	0.7356	0.0	0.0	1.5382E-01	0.7357	0.0	0.0
90	1.0	5.8982E-02	0.1050	5.8955E-02	0.1050	0.0	0.0	5.8977E-02	0.1050	0.0	0.0
90	0.9	5.9145E-02	0.2077	5.9119E-02	0.2077	0.0	0.0	5.9135E-02	0.2076	0.0	0.0
90	0.8	5.9963E-02	0.3172	5.9941E-02	0.3172	0.0	0.0	5.9945E-02	0.3172	0.0	0.0
90	0.7	6.1635E-02	0.4317	6.1616E-02	0.4317	0.0	0.0	6.1626E-02	0.4317	0.0	0.0
90	0.6	6.4483E-02	0.5485	6.4507E-02	0.5485	0.0	0.0	6.4505E-02	0.5485	0.0	0.0
90	0.5	6.9080E-02	0.6632	6.9076E-02	0.6632	0.0	0.0	6.9076E-02	0.6632	0.0	0.0
90	0.4	7.6106E-02	0.7705	7.6110E-02	0.7705	0.0	0.0	7.6107E-02	0.7705	0.0	0.0
90	0.3	8.6790E-02	0.8641	8.6793E-02	0.8641	0.0	0.0	8.6786E-02	0.8641	0.0	0.0
90	0.2	1.0266E-01	0.9372	1.0266E-01	0.9372	0.0	0.0	1.0265E-01	0.9372	0.0	0.0
90	0.1	1.2383E-01	0.9839	1.2382E-01	0.9839	0.0	0.0	1.2382E-01	0.9839	0.0	0.0
90	0.05	1.3428E-01	0.9960	1.3427E-01	0.9960	0.0	0.0	1.3426E-01	0.9959	0.0	0.0
180	1.0	5.8986E-02	0.1050	5.8955E-02	0.1050	-0.1	0.0	5.8978E-02	0.1049	0.0	0.0
180	0.9	7.1435E-02	0.0000	7.1410E-02	0.0000	0.0	0.0	7.1425E-02	0.0000	0.0	0.0
180	0.8	7.7524E-02	0.0186	7.7523E-02	0.0186	0.0	0.0	7.7532E-02	0.0186	0.0	0.0
180	0.7	8.3249E-02	0.0604	8.3216E-02	0.0604	0.0	0.0	8.3230E-02	0.0604	0.0	0.0
180	0.6	8.9419E-02	0.1174	8.9418E-02	0.1174	0.0	0.0	8.9424E-02	0.1175	0.0	0.0
180	0.5	9.6821E-02	0.1871	9.6823E-02	0.1871	0.0	0.0	9.6831E-02	0.1871	0.0	0.0
180	0.4	1.0632E-01	0.2684	1.0632E-01	0.2684	0.0	0.0	1.0632E-01	0.2684	0.0	0.0
180	0.3	1.1906E-01	0.3602	1.1905E-01	0.3602	0.0	0.0	1.1905E-01	0.3602	0.0	0.0
180	0.2	1.3628E-01	0.4614	1.3628E-01	0.4614	0.0	0.0	1.3627E-01	0.4614	0.0	0.0
180	0.1	1.5690E-01	0.5695	1.5692E-01	0.5695	0.0	0.0	1.5689E-01	0.5696	0.0	0.0
180	0.05	1.6549E-01	0.6250	1.6550E-01	0.6251	0.0	0.0	1.6548E-01	0.6250	0.0	0.0
MAX %						0.1	0.0			0.0	0.0
AVR %						0.0	0.0			0.0	0.0

Table 9a

Multiple scattering results for a uniform layer, OT=0.25, cos(SZA)=0.1

RAZ	cos(VZA)	MYSTIC: I	MYSTIC: P	MCSSA: I	MCSSA: P	dI, %	dP, %	VLIDORT: I	VLIDORT: P	dI, %	dP, %
0	1.0	2.6633E-02	0.8406	2.6628E-02	0.8405	0.0	0.0	2.6740E-02	0.8389	0.4	-0.2
0	0.9	3.2076E-02	0.6489	3.2058E-02	0.6490	-0.1	0.0	3.2197E-02	0.6478	0.4	-0.1
0	0.8	3.9947E-02	0.4523	3.9924E-02	0.4523	-0.1	0.0	4.0109E-02	0.4509	0.4	-0.1
0	0.7	4.9297E-02	0.3043	4.9293E-02	0.3044	0.0	0.0	4.9510E-02	0.3030	0.4	-0.1
0	0.6	6.0443E-02	0.1934	6.0422E-02	0.1936	0.0	0.0	6.0693E-02	0.1921	0.4	-0.1
0	0.5	7.3804E-02	0.1099	7.3801E-02	0.1099	0.0	0.0	7.4147E-02	0.1085	0.5	-0.1
0	0.4	9.0059E-02	0.0470	9.0075E-02	0.0470	0.0	0.0	9.0495E-02	0.0456	0.5	-0.1
0	0.3	1.0953E-01	0.0001	1.0955E-01	0.0001	0.0	0.0	1.1005E-01	0.0012	0.5	0.1
0	0.2	1.2946E-01	0.0337	1.2946E-01	0.0336	0.0	0.0	1.3003E-01	0.0348	0.4	0.1
0	0.1	1.2750E-01	0.0589	1.2751E-01	0.0589	0.0	0.0				
0	0.05	9.5780E-02	0.0742	9.5795E-02	0.0743	0.0	0.0				
90	1.0	2.6635E-02	0.8405	2.6628E-02	0.8405	0.0	0.0	2.6740E-02	0.8389	0.4	-0.2
90	0.9	2.9999E-02	0.8484	3.0006E-02	0.8485	0.0	0.0	3.0155E-02	0.8470	0.5	-0.1
90	0.8	3.4016E-02	0.8551	3.4012E-02	0.8551	0.0	0.0	3.4197E-02	0.8538	0.5	-0.1
90	0.7	3.8850E-02	0.8606	3.8859E-02	0.8606	0.0	0.0	3.9078E-02	0.8594	0.6	-0.1
90	0.6	4.4852E-02	0.8653	4.4847E-02	0.8653	0.0	0.0	4.5125E-02	0.8642	0.6	-0.1
90	0.5	5.2478E-02	0.8691	5.2485E-02	0.8692	0.0	0.0	5.2819E-02	0.8682	0.7	-0.1
90	0.4	6.2526E-02	0.8725	6.2510E-02	0.8726	0.0	0.0	6.2929E-02	0.8716	0.6	-0.1
90	0.3	7.6135E-02	0.8755	7.6130E-02	0.8756	0.0	0.0	7.6647E-02	0.8746	0.7	-0.1
90	0.2	9.4849E-02	0.8782	9.4862E-02	0.8781	0.0	0.0	9.5498E-02	0.8774	0.7	-0.1
90	0.1	1.1847E-01	0.8802	1.1844E-01	0.8803	0.0	0.0	1.1926E-01	0.8795	0.7	-0.1
90	0.05	1.2930E-01	0.8807	1.2930E-01	0.8806	0.0	0.0	1.3019E-01	0.8799	0.7	-0.1
180	1.0	2.6642E-02	0.8405	2.6628E-02	0.8405	-0.1	0.0	2.6740E-02	0.8389	0.4	-0.2
180	0.9	3.7351E-02	0.4636	3.7347E-02	0.4637	0.0	0.0	3.7527E-02	0.4615	0.5	-0.2
180	0.8	4.7789E-02	0.2779	4.7775E-02	0.2778	0.0	0.0	4.8028E-02	0.2757	0.5	-0.2
180	0.7	5.9631E-02	0.1567	5.9618E-02	0.1566	0.0	0.0	5.9926E-02	0.1546	0.5	-0.2
180	0.6	7.3640E-02	0.0729	7.3670E-02	0.0729	0.0	0.0	7.4028E-02	0.0711	0.5	-0.2
180	0.5	9.0990E-02	0.0142	9.1000E-02	0.0142	0.0	0.0	9.1438E-02	0.0124	0.5	-0.2
180	0.4	1.1338E-01	0.0264	1.1344E-01	0.0264	0.1	0.0	1.1396E-01	0.0282	0.5	0.2
180	0.3	1.4397E-01	0.0531	1.4400E-01	0.0532	0.0	0.0	1.4463E-01	0.0549	0.5	0.2
180	0.2	1.8756E-01	0.0685	1.8758E-01	0.0684	0.0	0.0	1.8837E-01	0.0701	0.4	0.2
180	0.1	2.4899E-01	0.0735	2.4900E-01	0.0735	0.0	0.0	2.4997E-01	0.0752	0.4	0.2
180	0.05	2.8418E-01	0.0726	2.8412E-01	0.0726	0.0	0.0	2.8511E-01	0.0742	0.3	0.2
MAX %						0.1	0.0			0.7	0.2
AVR %						0.0	0.0			0.5	0.1

Table 9b

Single scattering results for a uniform layer, OT=0.25, cos(SZA)=0.1.

RAZ	cos(VZA)	MYSTIC: I	MYSTIC: P	MCSSA: I	MCSSA: P	dI, %	dP, %	VLIDORT: I	VLIDORT: P	dI, %	dP, %
0	1.0	1.9253E-02	0.9802	1.9261E-02	0.9802	0.0	0.0	1.9261E-02	0.9802	0.0	0.0
0	0.9	2.3021E-02	0.7887	2.3017E-02	0.7887	0.0	0.0	2.3024E-02	0.7887	0.0	0.0
0	0.8	2.8651E-02	0.5782	2.8638E-02	0.5782	0.0	0.0	2.8647E-02	0.5782	0.0	0.0
0	0.7	3.5367E-02	0.4181	3.5378E-02	0.4181	0.0	0.0	3.5375E-02	0.4182	0.0	0.0
0	0.6	4.3429E-02	0.2973	4.3431E-02	0.2973	0.0	0.0	4.3425E-02	0.2973	0.0	0.0
0	0.5	5.3162E-02	0.2057	5.3168E-02	0.2057	0.0	0.0	5.3167E-02	0.2057	0.0	0.0
0	0.4	6.5084E-02	0.1362	6.5090E-02	0.1362	0.0	0.0	6.5088E-02	0.1362	0.0	0.0
0	0.3	7.9469E-02	0.0841	7.9479E-02	0.0841	0.0	0.0	7.9475E-02	0.0841	0.0	0.0
0	0.2	9.4327E-02	0.0461	9.4338E-02	0.0461	0.0	0.0	9.4333E-02	0.0462	0.0	0.0
0	0.1	9.2025E-02	0.0202	9.2043E-02	0.0202	0.0	0.0				
0	0.05	6.6337E-02	0.0113	6.6338E-02	0.0113	0.0	0.0				
90	1.0	1.9264E-02	0.9802	1.9261E-02	0.9802	0.0	0.0	1.9261E-02	0.9802	0.0	0.0
90	0.9	2.1107E-02	0.9839	2.1108E-02	0.9839	0.0	0.0	2.1111E-02	0.9839	0.0	0.0
90	0.8	2.3364E-02	0.9873	2.3361E-02	0.9873	0.0	0.0	2.3361E-02	0.9873	0.0	0.0
90	0.7	2.6151E-02	0.9902	2.6151E-02	0.9902	0.0	0.0	2.6147E-02	0.9902	0.0	0.0
90	0.6	2.9683E-02	0.9928	2.9681E-02	0.9928	0.0	0.0	2.9681E-02	0.9928	0.0	0.0
90	0.5	3.4278E-02	0.9950	3.4274E-02	0.9950	0.0	0.0	3.4279E-02	0.9950	0.0	0.0
90	0.4	4.0449E-02	0.9968	4.0439E-02	0.9968	0.0	0.0	4.0449E-02	0.9968	0.0	0.0
90	0.3	4.8986E-02	0.9982	4.8990E-02	0.9982	0.0	0.0	4.8990E-02	0.9982	0.0	0.0
90	0.2	6.0952E-02	0.9992	6.0961E-02	0.9992	0.0	0.0	6.0957E-02	0.9992	0.0	0.0
90	0.1	7.6252E-02	0.9998	7.6236E-02	0.9998	0.0	0.0	7.6250E-02	0.9998	0.0	0.0
90	0.05	8.3221E-02	0.9999	8.3218E-02	1.0000	0.0	0.0	8.3221E-02	0.9999	0.0	0.0
180	1.0	1.9260E-02	0.9802	1.9261E-02	0.9802	0.0	0.0	1.9261E-02	0.9802	0.0	0.0
180	0.9	2.7111E-02	0.5695	2.7111E-02	0.5695	0.0	0.0	2.7112E-02	0.5696	0.0	0.0
180	0.8	3.4678E-02	0.3714	3.4669E-02	0.3714	0.0	0.0	3.4679E-02	0.3714	0.0	0.0
180	0.7	4.3248E-02	0.2428	4.3230E-02	0.2428	0.0	0.0	4.3243E-02	0.2428	0.0	0.0
180	0.6	5.3406E-02	0.1543	5.3398E-02	0.1543	0.0	0.0	5.3399E-02	0.1542	0.0	0.0
180	0.5	6.5957E-02	0.0922	6.5950E-02	0.0922	0.0	0.0	6.5956E-02	0.0922	0.0	0.0
180	0.4	8.2221E-02	0.0492	8.2247E-02	0.0492	0.0	0.0	8.2229E-02	0.0492	0.0	0.0
180	0.3	1.0445E-01	0.0211	1.0449E-01	0.0211	0.0	0.0	1.0445E-01	0.0211	0.0	0.0
180	0.2	1.3622E-01	0.0051	1.3622E-01	0.0051	0.0	0.0	1.3619E-01	0.0051	0.0	0.0
180	0.1	1.8071E-01	0.0000	1.8069E-01	0.0000	0.0	0.0	1.8068E-01	0.0000	0.0	0.0
180	0.05	2.0565E-01	0.0013	2.0566E-01	0.0013	0.0	0.0	2.0563E-01	0.0013	0.0	0.0
MAX %						0.0	0.0			0.0	0.0
AVR %						0.0	0.0			0.0	0.0

Table 10a

Multiple scattering results for a layer with profile, OT=0.25, cos(SZA)=0.1.

RAZ	cos(VZA)	MYSTIC: I	MYSTIC: P	MCSSA: I	MCSSA: P	dI, %	dP, %	VLIDORT: I	VLIDORT: P	dI, %	dP, %
0	1.0	2.3461E-02	0.8588	2.3470E-02	0.8588	0.0	0.0	2.3554E-02	0.8575	0.4	-0.1
0	0.9	2.8249E-02	0.6674	2.8237E-02	0.6674	0.0	0.0	2.8342E-02	0.6664	0.3	-0.1
0	0.8	3.5196E-02	0.4688	3.5181E-02	0.4688	0.0	0.0	3.5319E-02	0.4677	0.4	-0.1
0	0.7	4.3466E-02	0.3193	4.3468E-02	0.3193	0.0	0.0	4.3628E-02	0.3182	0.4	-0.1
0	0.6	5.3328E-02	0.2070	5.3337E-02	0.2071	0.0	0.0	5.3538E-02	0.2059	0.4	-0.1
0	0.5	6.5217E-02	0.1224	6.5237E-02	0.1224	0.0	0.0	6.5497E-02	0.1213	0.4	-0.1
0	0.4	7.9761E-02	0.0586	7.9776E-02	0.0586	0.0	0.0	8.0086E-02	0.0575	0.4	-0.1
0	0.3	9.7247E-02	0.0110	9.7249E-02	0.0110	0.0	0.0	9.7628E-02	0.0099	0.4	-0.1
0	0.2	1.1525E-01	0.0234	1.1523E-01	0.0233	0.0	0.0	1.1567E-01	0.0243	0.4	0.1
0	0.1	1.1309E-01	0.0486	1.1312E-01	0.0486	0.0	0.0				
0	0.05	8.3505E-02	0.0632	8.3490E-02	0.0631	0.0	0.0				
90	1.0	2.3469E-02	0.8587	2.3470E-02	0.8588	0.0	0.0	2.3554E-02	0.8575	0.4	-0.1
90	0.9	2.6372E-02	0.8657	2.6365E-02	0.8658	0.0	0.0	2.6474E-02	0.8646	0.4	-0.1
90	0.8	2.9806E-02	0.8717	2.9808E-02	0.8716	0.0	0.0	2.9945E-02	0.8705	0.5	-0.1
90	0.7	3.4004E-02	0.8765	3.3994E-02	0.8765	0.0	0.0	3.4154E-02	0.8755	0.4	-0.1
90	0.6	3.9191E-02	0.8806	3.9188E-02	0.8807	0.0	0.0	3.9390E-02	0.8797	0.5	-0.1
90	0.5	4.5857E-02	0.8841	4.5841E-02	0.8841	0.0	0.0	4.6085E-02	0.8833	0.5	-0.1
90	0.4	5.4631E-02	0.8872	5.4626E-02	0.8871	0.0	0.0	5.4930E-02	0.8863	0.5	-0.1
90	0.3	6.6619E-02	0.8897	6.6628E-02	0.8898	0.0	0.0	6.7005E-02	0.8890	0.6	-0.1
90	0.2	8.3248E-02	0.8921	8.3252E-02	0.8921	0.0	0.0	8.3715E-02	0.8914	0.6	-0.1
90	0.1	1.0429E-01	0.8940	1.0427E-01	0.8939	0.0	0.0	1.0488E-01	0.8933	0.6	-0.1
90	0.05	1.1385E-01	0.8943	1.1386E-01	0.8943	0.0	0.0	1.1451E-01	0.8936	0.6	-0.1
180	1.0	2.3466E-02	0.8589	2.3470E-02	0.8588	0.0	0.0	2.3554E-02	0.8575	0.4	-0.1
180	0.9	3.2947E-02	0.4773	3.2951E-02	0.4774	0.0	0.0	3.3083E-02	0.4757	0.4	-0.2
180	0.8	4.2182E-02	0.2901	4.2169E-02	0.2899	0.0	0.0	4.2359E-02	0.2882	0.4	-0.2
180	0.7	5.2654E-02	0.1677	5.2656E-02	0.1677	0.0	0.0	5.2880E-02	0.1662	0.4	-0.2
180	0.6	6.5111E-02	0.0835	6.5111E-02	0.0835	0.0	0.0	6.5372E-02	0.0819	0.4	-0.2
180	0.5	8.0520E-02	0.0243	8.0508E-02	0.0243	0.0	0.0	8.0827E-02	0.0228	0.4	-0.1
180	0.4	1.0046E-01	0.0166	1.0050E-01	0.0167	0.0	0.0	1.0087E-01	0.0181	0.4	0.2
180	0.3	1.2775E-01	0.0437	1.2781E-01	0.0438	0.0	0.0	1.2825E-01	0.0451	0.4	0.1
180	0.2	1.6682E-01	0.0591	1.6685E-01	0.0591	0.0	0.0	1.6741E-01	0.0604	0.4	0.1
180	0.1	2.2167E-01	0.0642	2.2173E-01	0.0642	0.0	0.0	2.2241E-01	0.0655	0.3	0.1
180	0.05	2.5256E-01	0.0632	2.5254E-01	0.0632	0.0	0.0	2.5322E-01	0.0644	0.3	0.1
MAX %						0.0	0.0			0.6	0.2
AVR %						0.0	0.0			0.4	0.1

Table 10b

Single scattering results for a layer with profile, OT=0.25, cos(SZA)=0.1

RAz	cos(VZA)	MYSTIC: I	MYSTIC: P	MCSSA: I	MCSSA: P	dl, %	dP, %	VLDORT: I	VLDORT: P	dl, %	dP, %
0	1.0	1.7692E-02	0.9802	1.7697E-02	0.9802	0.0	0.0	1.7698E-02	0.9802	0.0	0.0
0	0.9	2.1168E-02	0.7887	2.1157E-02	0.7887	-0.1	0.0	2.1164E-02	0.7887	0.0	0.0
0	0.8	2.6347E-02	0.5782	2.6338E-02	0.5782	0.0	0.0	2.6348E-02	0.5782	0.0	0.0
0	0.7	3.2564E-02	0.4181	3.2558E-02	0.4181	0.0	0.0	3.2556E-02	0.4182	0.0	0.0
0	0.6	4.0000E-02	0.2973	4.0000E-02	0.2973	0.0	0.0	3.9997E-02	0.2973	0.0	0.0
0	0.5	4.9020E-02	0.2057	4.9020E-02	0.2057	0.0	0.0	4.9020E-02	0.2057	0.0	0.0
0	0.4	6.0081E-02	0.1362	6.0097E-02	0.1362	0.0	0.0	6.0092E-02	0.1362	0.0	0.0
0	0.3	7.3508E-02	0.0841	7.3510E-02	0.0841	0.0	0.0	7.3505E-02	0.0841	0.0	0.0
0	0.2	8.7417E-02	0.0461	8.7433E-02	0.0461	0.0	0.0	8.7428E-02	0.0462	0.0	0.0
0	0.1	8.5144E-02	0.0202	8.5145E-02	0.0202	0.0	0.0				
0	0.05	6.0592E-02	0.0113	6.0592E-02	0.0113	0.0	0.0				
90	1.0	1.7702E-02	0.9802	1.7697E-02	0.9802	0.0	0.0	1.7698E-02	0.9802	0.0	0.0
90	0.9	1.9403E-02	0.9839	1.9403E-02	0.9839	0.0	0.0	1.9406E-02	0.9839	0.0	0.0
90	0.8	2.1484E-02	0.9873	2.1484E-02	0.9873	0.0	0.0	2.1485E-02	0.9873	0.0	0.0
90	0.7	2.4056E-02	0.9902	2.4065E-02	0.9902	0.0	0.0	2.4062E-02	0.9902	0.0	0.0
90	0.6	2.7336E-02	0.9928	2.7335E-02	0.9928	0.0	0.0	2.7335E-02	0.9928	0.0	0.0
90	0.5	3.1606E-02	0.9950	3.1597E-02	0.9950	0.0	0.0	3.1602E-02	0.9950	0.0	0.0
90	0.4	3.7335E-02	0.9968	3.7334E-02	0.9968	0.0	0.0	3.7341E-02	0.9968	0.0	0.0
90	0.3	4.5311E-02	0.9982	4.5310E-02	0.9982	0.0	0.0	4.5311E-02	0.9982	0.0	0.0
90	0.2	5.6524E-02	0.9992	5.6522E-02	0.9992	0.0	0.0	5.6518E-02	0.9992	0.0	0.0
90	0.1	7.0873E-02	0.9998	7.0861E-02	0.9998	0.0	0.0	7.0875E-02	0.9998	0.0	0.0
90	0.05	7.7375E-02	1.0000	7.7369E-02	0.9999	0.0	0.0	7.7374E-02	0.9999	0.0	0.0
180	1.0	1.7697E-02	0.9802	1.7697E-02	0.9802	0.0	0.0	1.7698E-02	0.9802	0.0	0.0
180	0.9	2.4923E-02	0.5695	2.4919E-02	0.5695	0.0	0.0	2.4920E-02	0.5695	0.0	0.0
180	0.8	3.1900E-02	0.3714	3.1881E-02	0.3714	-0.1	0.0	3.1890E-02	0.3714	0.0	0.0
180	0.7	3.9793E-02	0.2428	3.9780E-02	0.2428	0.0	0.0	3.9788E-02	0.2428	0.0	0.0
180	0.6	4.9159E-02	0.1543	4.9168E-02	0.1543	0.0	0.0	4.9168E-02	0.1542	0.0	0.0
180	0.5	6.0783E-02	0.0922	6.0781E-02	0.0922	0.0	0.0	6.0785E-02	0.0922	0.0	0.0
180	0.4	7.5878E-02	0.0492	7.5892E-02	0.0492	0.0	0.0	7.5873E-02	0.0492	0.0	0.0
180	0.3	9.6516E-02	0.0211	9.6556E-02	0.0211	0.0	0.0	9.6526E-02	0.0211	0.0	0.0
180	0.2	1.2610E-01	0.0051	1.2611E-01	0.0051	0.0	0.0	1.2609E-01	0.0051	0.0	0.0
180	0.1	1.6746E-01	0.0000	1.6746E-01	0.0000	0.0	0.0	1.6746E-01	0.0000	0.0	0.0
180	0.05	1.9035E-01	0.0013	1.9036E-01	0.0013	0.0	0.0	1.9033E-01	0.0013	0.0	0.0
MAX %						0.1	0.0			0.0	0.0
AVR %						0.0	0.0			0.0	0.0

Table 11aAbsolute maximum (and average) values of the percentile deviations in TOA-reflected multiple scattering intensity I and degree of linear polarization P , Eq. (4), between spherical RT values and strict plane-parallel atmosphere results. "Uniform" and "profile" correspond to $g = 0$ and 1, respectively, in Eq. (1).

atmosphere	\approx SZA, deg.	OT=1: dl, %	OT=0.25: dl, %	OT=1: dP, %	OT=0.25: dP, %
uniform	25.84	2.2 (0.9)	18 (5)	5.2 (0.7)	1.6 (0.2)
uniform	84.26	89 (16)	34 (13)	6.8 (1.1)	2.9 (0.3)
profile	25.84	17 (4)	24 (6)	2.8 (0.3)	1.5 (0.2)
profile	84.26	94 (15)	43 (13)	4.0 (0.5)	2.5 (0.3)

Table 11b

same as Table 11(a) except for VLDORT's pseudospherical correction (VLPS).

atmosphere	\approx SZA, deg.	OT=1: dl, %	OT=0.25: dl, %	OT=1: dP, %	OT=0.25: dP, %
uniform	25.84	5.9 (1.1)	4.4 (1.4)	3.4 (0.4)	1.8 (0.4)
uniform	84.26	37.7 (6.0)	10.5 (2.0)	4.9 (0.7)	2.2 (0.4)
profile	25.84	3.0 (1.1)	4.8 (1.4)	1.4 (0.3)	1.9 (0.3)
profile	84.26	30.0 (4.6)	9.7 (1.9)	4.7 (0.7)	2.1 (0.4)

Table 11c

same as Table 11(a) except for VLDORT's multipoint spherical correction (VLSC).

atmosphere	\approx SZA, deg.	OT=1: dl, %	OT=0.25: dl, %	OT=1: dP, %	OT=0.25: dP, %
uniform	25.84	0.2 (0.1)	0.2 (0.1)	0.1 (0.0)	0.1 (0.0)
uniform	84.26	0.2 (0.1)	0.7 (0.5)	0.2 (0.1)	0.2 (0.1)
profile	25.84	0.1 (0.0)	0.1 (0.1)	0.0 (0.0)	0.1 (0.0)
profile	84.26	0.1 (0.0)	0.6 (0.4)	0.1 (0.0)	0.2 (0.1)

and view μ zenith angles, and relative azimuth φ); (b) the effect of sphericity is more pronounced at lower optical depth (see, e.g., Figs. 2 and 3 for OT = 0.25 and 1, respectively, in A&K); and (c) if absorption is negligible, single-to-multiple scattering ratios for spherical and plane-parallel atmospheres are quite close (within the accuracy of their MC code). The latter observation suggests one way to approximate multiple scattering in spherical atmospheres, namely to use plane parallel calculations of the single-to-multiple scattering ratios, and use these alongside accurate single-scatter full-spherical simulations. A&K limited themselves to scattering in the principal plane, which we have extended [14]. However, both these papers ignored vertical variations of optical properties and polarization of light, the latter being very important for Rayleigh scattering at the abovementioned wavelengths [21].

This situation with reliable benchmarks has changed drastically in the past year, with the advent of several new papers in the literature. Zawada et al. [29] numerically compared seven spherical RT codes (four MC and three deterministic) in limb scattering geometry, at eleven

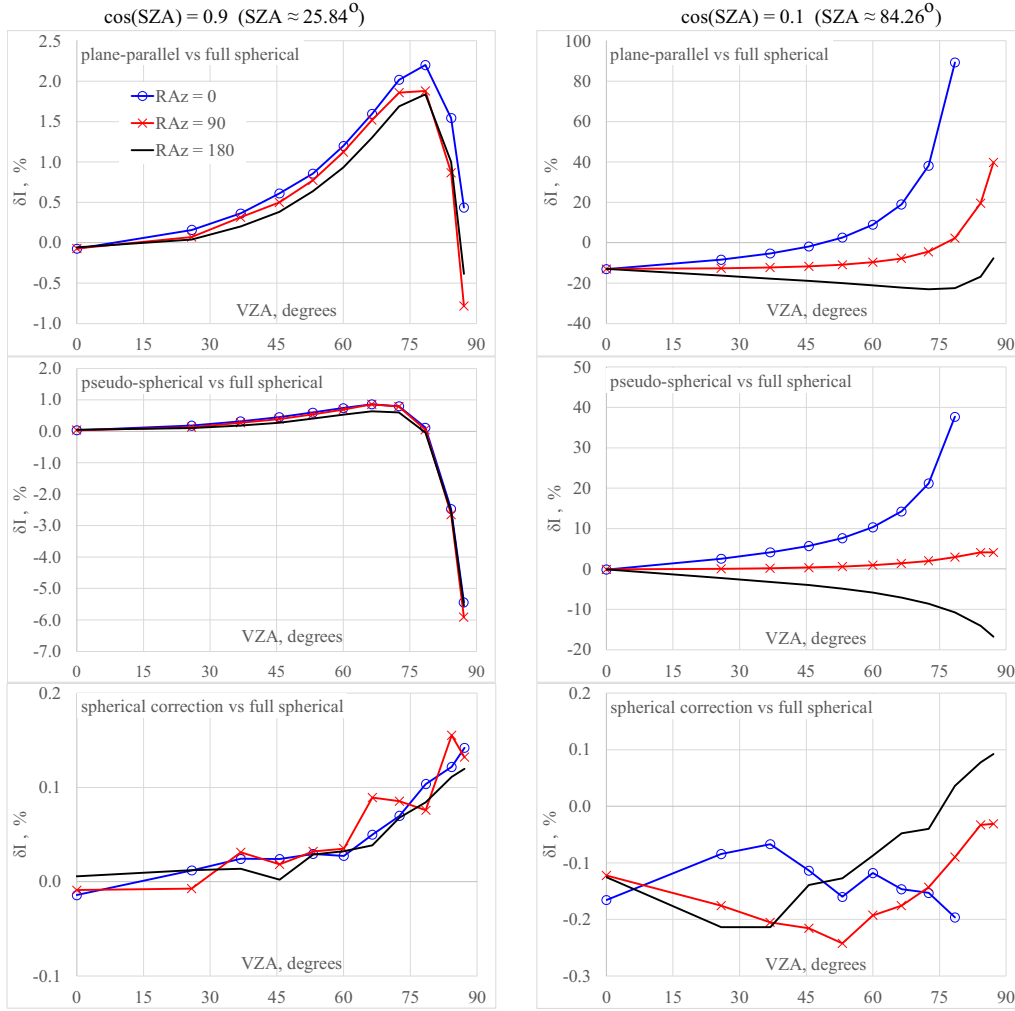


Fig. 1. Relative deviation for intensity, I , as function of solar/view geometry for a uniform atmosphere, $g = 0$ in Eq. (1), and total OT = 1. Rows compare results with VLIDORT plane-parallel (top), pseudo-spherical (middle), and spherical correction (bottom) against full-spherical MC baselines. In the bottom row, the MC noise is $\sim 0.1\%$, which becomes visible thanks to the excellent agreement between VLIDORT's multipoint spherical correction and MYSTIC's full spherical solution. Refer to Table 2b for clarification regarding the two missing points, $\cos(VZA) = 0.1$ and 0.05 , for $\cos(SZA) = 0.1$ (right column) at $RAz = 0^\circ$ (blue line, circle marker).

wavelengths from 300 (nm) to 1700 (nm). In addition to pure Rayleigh, they considered absorption profiles and aerosol-Rayleigh mixtures, multiple solar/view geometries, and different tangent heights, dark and reflecting Lambertian surfaces, and atmospheric refraction (in 4 of the models). The RT models participating in this study showed agreement to within 0.2% and 1% in single and multiple scattering computations, respectively. Moreover, this paper also reported runtimes for the 7 codes and included the effect of light polarization. Rozanov et al. [22] developed an approximate technique to solve the RT equation including first-order rotational Raman scattering in a spherical atmosphere. This technique was implemented in the RT model SCIATRAN for both limb and non-limb geometries. Although this paper discusses the theoretical background in detail, the authors do not present convenient numerical benchmarks. In order to reproduce their result, it is necessary to install and run the whole SCIATRAN package. A&K initially discovered that the ratio of multiple to single scattering contribution in a spherical atmosphere is approximately the same as that of the atmosphere in the plane-parallel geometry. Based on this and on the assumption of equity of the degree of polarization in both geometries, Zhai and Hu [30] developed an improved pseudo spherical shell approximation for spherical shell atmosphere (see their Eqs. (7a-d)).

Away from the atmospheric science field, Garcia [10] solves the problem of neutron transport for a scattering spherical medium with internal sources and external incident flux, using the method of spherical harmonics in spherical geometry [12]. Numerous tables contain results for the (scalar) flux at different levels in the sphere, along with convergence of the method, and the runtimes. The Open Neutron Transport Package (OpenNTP), an open-source scholar-driven tool for computer analysis of nuclear reactors, simulates the angular-dependence of neutron fluxes as they propagate in a spherical medium, among other geometries available in the package [15]. However, interpretation of neutron scattering results for our light scattering applications is not always straightforward.

Several older, but still valuable, papers have come to our attention as we updated our literature review for this manuscript. Hummer et al. [11] presented a source code, in FORTRAN IV, and theoretical background for multiple scattering of radiation in a spherically symmetric stellar atmosphere surrounding a central core that emits and absorbs radiation. Spagna and Leung [23] describe their source code for RT in spherically symmetric dust clouds covering stars, a scenario also considered by van de Hulst [27,28]. Christensen [4] reports numerical results for neutron transport in a spherical medium using MC method. Lary and Balluch [16] discuss the importance of spherical geometry for simulation of the Earth heat rates in global circulation (GCM) models.

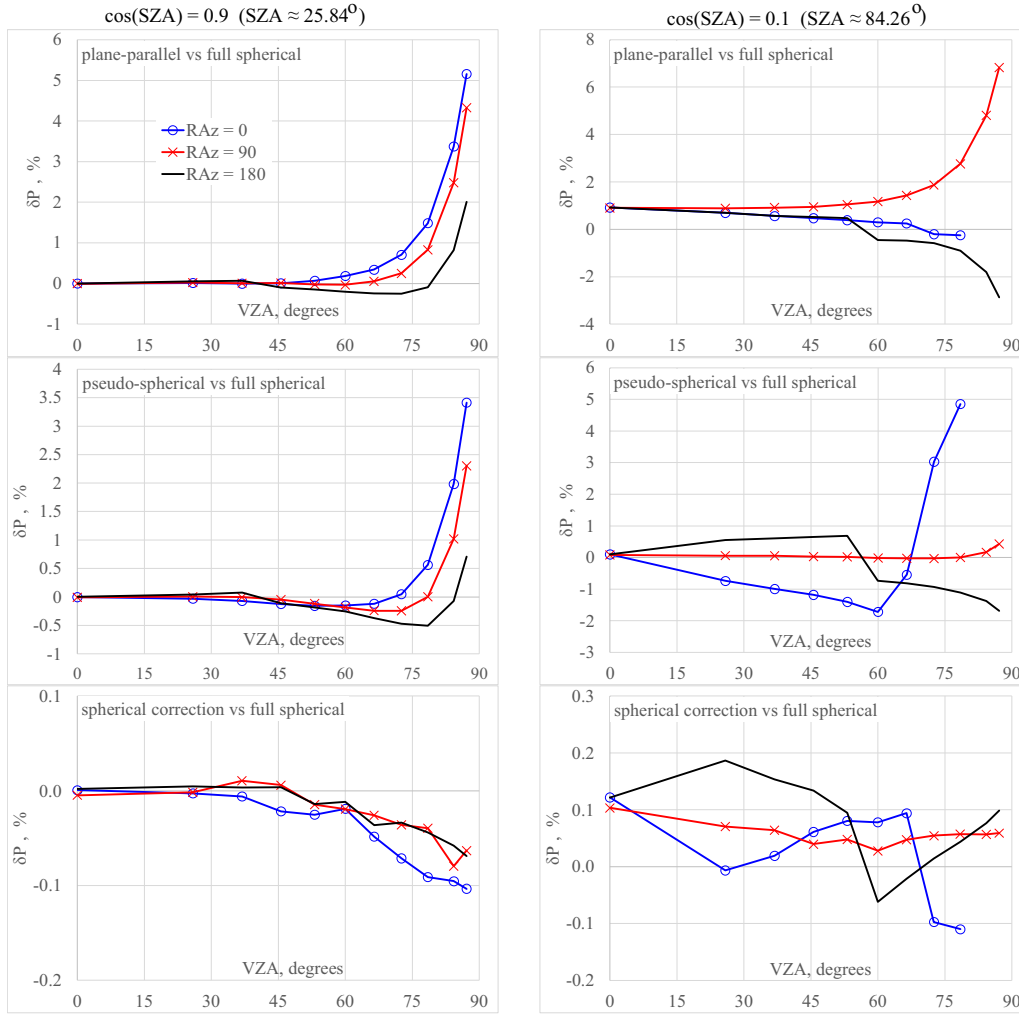


Fig. 2. Relative deviations for the degree of linear polarization, P , as function of solar/view geometry for the uniform atmosphere scenario, $g = 0$ in Eq. (1), and total $OT = 1$. Rows compare results with VLIDORT plane-parallel (top), pseudo-spherical (middle), and spherical correction (bottom) against full-spherical MC baselines. Refer to Table 2b for clarification regarding the two missing points, $\cos(VZA) = 0.1$ and 0.05 , for $\cos(SZA) = 0.1$ (right column) at $RAz = 0^\circ$ (blue line, circle marker).

To further support the development of tools for numerical simulation of RT in the spherical Earth atmosphere medium, we aim in this paper to extend our previous results and consider polarization of light and vertical profile in atmosphere. At the same time, we attempt to offer benchmarks which are easy to understand and reproduce by those who use or develop spherical RT code. For this reason, we have remained within a simple scenario (as compared to, e.g., Zawada et al. [29]), namely, that of a Rayleigh scattering atmosphere with zero depolarization factor, $\delta = 0$ [21]: Eqs. (7)–(8), over a dark surface.

Specifically, we pursue three goals which emerged from our previous work [14]: in particular see the concluding remarks. These are: (a) to provide reliable numerical benchmarks for the validation of existing and future spherical RT codes (especially those using approximations) that account for the effect of polarization of light; (b) to consider an inhomogeneous atmosphere, with optical properties of which change with the radius height; and (c) to better understand the influence of atmospheric curvature on the signal of a spaceborne polarimeter. We solve (a) and (b) for non-limb geometry. In the sections below, our reader will find methodology, numerical and graphical results, and a brief conclusion.

2. Methodology

An ideal scenario to meet our goals was considered by Michael Mishchenko back in the 1990's [20]. In that paper, he extended the invariant imbedding method to include polarization and developed a vector (polarized) RT code. Using this code, he published accurate numerical results for the angular distribution of polarized light reflected from a plane-parallel Rayleigh scattering atmosphere, without depolarization, over a dark surface with exponentially varying gaseous absorber:

$$\omega_0(\tau) = \exp(-g\tau). \quad (1)$$

In Eq. (1), ω_0 is the single scattering albedo (SSA), $g = 0, 0.001, 0.01, 0.1$, and 1 is a decay factor, and τ is optical thickness (OT); $\tau = 0$ and $\tau = 1$ correspond to top (TOA) and bottom (BOA) of atmosphere, respectively. The value $g = 0$ yields a uniform layer with no absorption. Eq. (1) is not typical for atmosphere of the Earth, but it is convenient for validation of RT codes in optically inhomogeneous media.

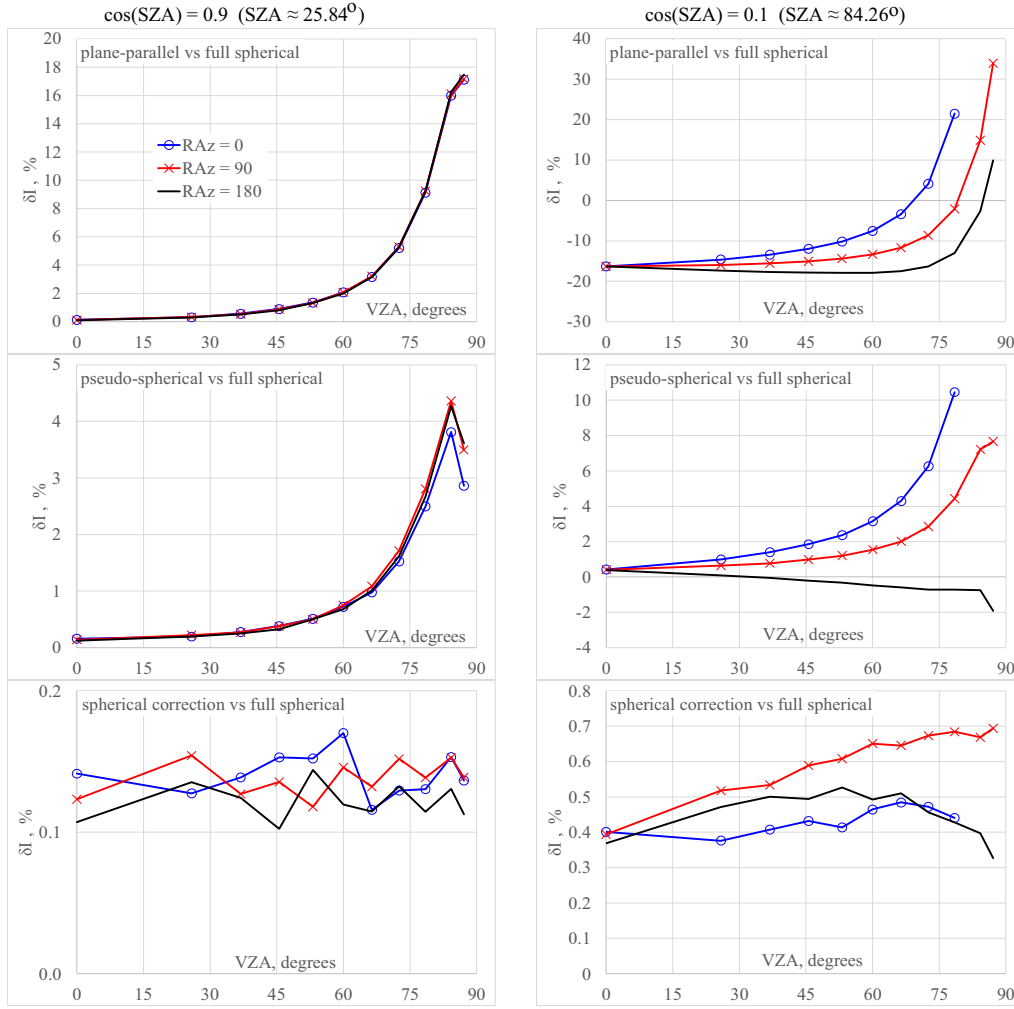


Fig. 3. Relative deviations for intensity, I , as function of solar/view geometry for the uniform atmosphere case, $g = 0$ in Eq. (1), and total OT = 0.25. Rows compare results with VLIDORT plane-parallel (top), pseudo-spherical (middle), and spherical correction (bottom) against full-spherical MC baselines. Refer to Table 2b for clarification regarding the two missing points, $\cos(VZA) = 0.1$ and 0.05 , for $\cos(SZA) = 0.1$ (right column) at $RAz = 0^\circ$ (blue line, circle marker).

Mishchenko [20] selected the solar zenith angle (SZA), view zenith angle (VZA), and relative azimuth (RAz) angle as follows:

$$\cos(SZA) = 0.9; SZA \approx 25.84^\circ;$$

$$\cos(VZA) = 0.05, 0.1, 0.2, \dots, 0.9, 1.0 (11 \text{ values total});$$

$$RAz = 0^\circ, 90^\circ, 180^\circ.$$

(2)

where $SZA = 0^\circ$ indicates the overhead Sun; all VZAs correspond to radiation going from the Earth towards the space (upward); $\cos(VZA) = 1$ is the nadir, $\cos(VZA) = 0.05$ approaches the horizon; $RAz = 0^\circ$ indicates forward scattering. These results have become benchmarks for vector RT codes - e.g., see “Rayleigh scattering” section under “Benchmark results” on the IPRT website¹ or [13]: p.307, Tests 37-40. Mishchenko also demonstrated the importance of polarization in radiance calculations for Rayleigh-scattering atmosphere [21]. He showed that the radiance error from the neglect of polarization reaches a maximum value of about 10% at OT ≈ 1 in the case of pure Rayleigh scattering.

In contrast with the plane-parallel case, defining the solar/view geometry, Eq. (2), in a spherical atmosphere depends on a given location (see Fig. 2 and Appendix 2 in [14]). In our previous study, we defined the solar/view geometry at TOA, following the A&K convention. In this paper, we choose to define all angles at BOA for the following reasons: a) BOA is at ground level, which is a strictly defined boundary, while choice of the TOA height is to some extent arbitrary; b) satellite Level-1 geolocation data include solar/view angles defined at BOA (e.g., see Figs. 2 and 3 on the USGS website for Landsat²).

Therefore, by considering the scenario Eq. (1), we can illustrate numerically the influence of the Earth's sphericity on the reflected intensity and polarization, as compared to the plane-parallel case, under optical conditions where polarization is important. However, following A&K, we include OT = 0.25, because the effect of atmospheric curvature is more pronounced at smaller optical depth as the zenith angle reaches the horizon. We also consider $\cos(SZA) = 0.1$ ($SZA \approx 84.26^\circ$) in addition to Mishchenko's $\cos(SZA) = 0.9$ ($SZA \approx$

¹ <https://www.meteo.physik.uni-muenchen.de/~iprt> (accessed 04/01/2022)

² <https://www.usgs.gov/core-science-systems/nli/landsat/solar-illumination-and-sensor-viewing-angle-coefficient-files> (accessed 04/01/2022)

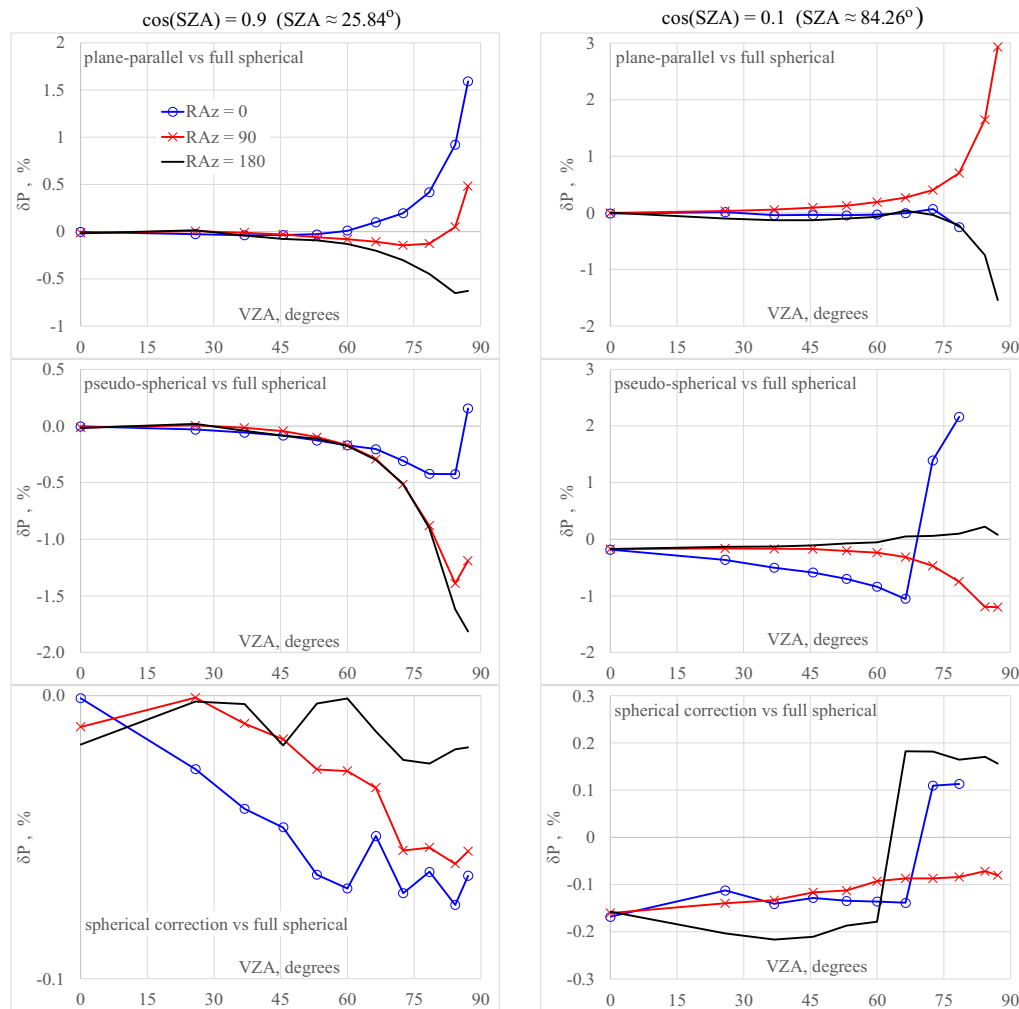


Fig. 4. Relative deviations for degree of linear polarization, P , as function of solar/view geometry for the uniform atmosphere case, $g = 0$ in Eq. (1), and total OT = 0.25. Rows compare results with VLIDORT plane-parallel (top), pseudo-spherical (middle), and spherical correction (bottom) against full-spherical MC baselines. Refer to Table 2b for clarification regarding the two missing points, $\cos(\text{VZA}) = 0.1$ and 0.05 , for $\cos(\text{SZA}) = 0.1$ (right column) at $\text{RAz} = 0^\circ$ (blue line, circle marker).

25.84°) to show the effect of low sun angle closer to the horizon and to be consistent with A&K and the scenarios used in our previous paper.

We report numerical data for single and multiple (including single) scattering³ separately. We limit ourselves to $g = 0$ (a uniform layer without absorption, like A&K, but with polarization) and $g = 1$ (strongest height dependence) in Eq. (1). The choice of an atmosphere with constant layer OT is designed to characterize the ability of the VLIDORT model (with and without its spherical corrections) to handle spherical scenarios. The same atmosphere was used in the original scalar RT comparisons in our previous paper [14]. The case with absorption, $g = 1$, allows one to check the accuracy of the approximate spherical RT model based on scaling plane-parallel multiple scattering (recall: each scattering orders 'S' depends on ω_0^S ; all orders are equally weighted only in the conservative case) by the ratio of single scattering fields for spherical and plane-parallel approximations (ω_0 cancels out in this ratio).

For numerical simulation, the continuous height-dependence in Eq. (1) must be discretized. In the invariant embedding method, it is possible to vary the integration step [20]: Sec. 4.5. Atmosphere layers close to TOA have the most significant effect on the reflected radiation, hence smaller height discretization steps are required in these locations. Lower in the atmosphere, a larger step size can be used, which will decrease computation time without accuracy loss. However, in this study, we split the atmosphere into $N_L = 100$ layers of the same geometric thickness, $dz = 1\text{ km}$, where N_L denotes the number of layers ($N_B = 101$ is the number of boundaries). This definition yields a smooth change of the solar/view geometry as a function of height and maintains the desired accuracy; computation speed is less of an issue when generating benchmark numbers. Further, $N_L = 100$ layers is consistent with the scenario used in our previous study, and also with the heritage ozone retrievals from the TOMS and OMI missions. We also assume the same total optical thickness for each homogeneous step-layer dz , and we compute scattering and absorbing optical thickness values from Eq. (1) – see Table 1 for OTs = 0.25 and 1. We also tabulate SSA values for the 10 top and 10 bottom step-layers $dz = 1\text{ km}$, for reference. All $N_L = 100$ values for scattering and absorption OTs are available from the journal's website in Excel format. For every step-layer $dz = 1\text{ km}$, the single scattering albedo is an average of values at the two boundaries.

³ Literature does not impose strict requirement on the inclusion or exclusion of single from multiple scattering. Our definition of multiple scattering (including single) is the same as "total scattering" in A&K.

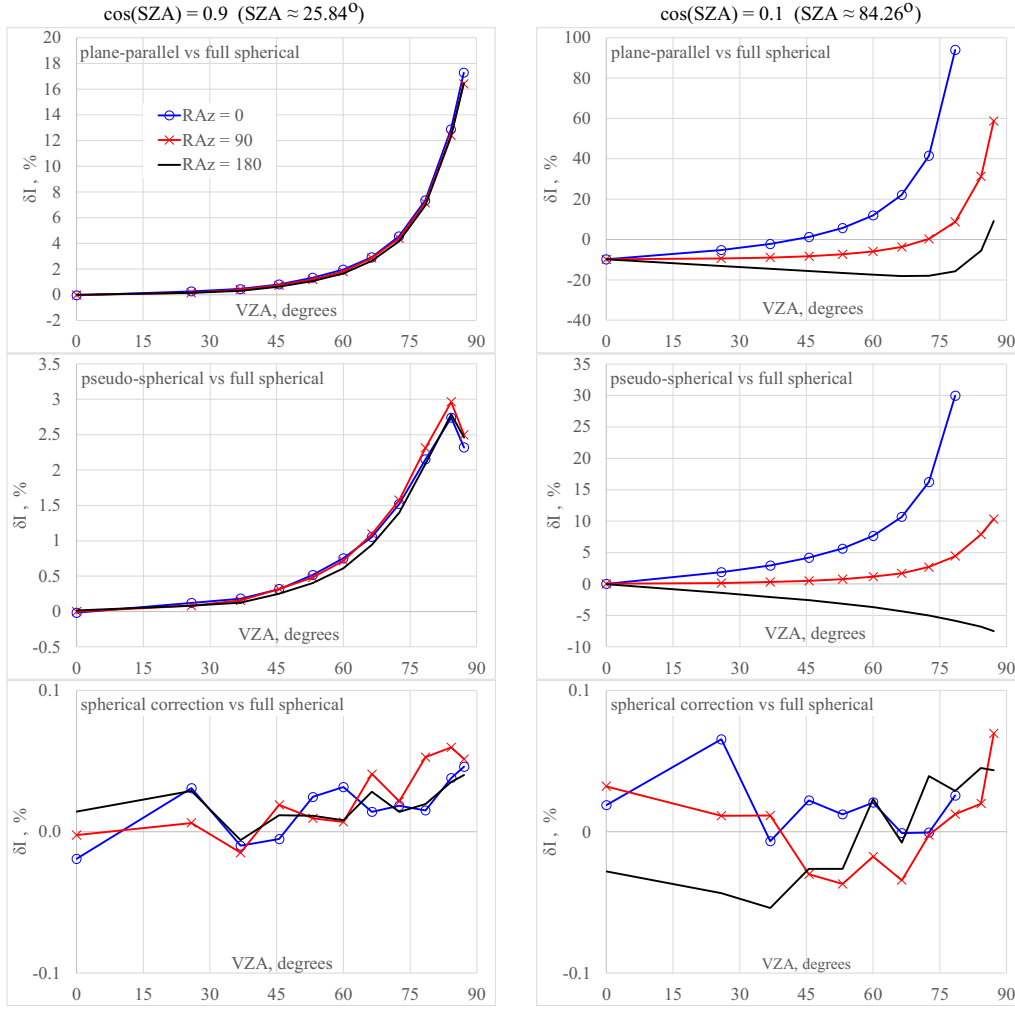


Fig. 5. Relative deviations for intensity, I , as function of solar/view geometry for the scenario with and absorption profile, $g = 1$ in Eq. (1), and total OT = 1. Rows compare results with VLIDORT plane-parallel (top), pseudo-spherical (middle), and spherical correction (bottom) against full-spherical MC baselines. Refer to Table 2b for clarification regarding the two missing points, $\cos(VZA) = 0.1$ and 0.05 , for $\cos(SZA) = 0.1$ (right column) at $RAz = 0^\circ$ (blue line, circle marker).

In order to achieve numerical accuracy to within a fraction of percent (typical for RT simulations [14,29,31]), we use three state-of-the-art RT codes. Two are MC codes: the Monte Carlo code MYSTIC [6,7,19] which is operated as one of the radiative transfer solvers of the libRadtran package [8,18], and the MC code for Spherical Shell Atmosphere (MCSSA) [30]. They both simulate light scattering in a true-spherical atmosphere using the backward MC technique enhanced with local estimation. MCSSA is based on the code by A&K [1]; however, their original code has undergone significant refactoring.

In [31] and [14] it was confirmed that using 100 million (100M) photons in MYSTIC resulted in errors not exceeding 0.1%. We keep this number of photons for both MC codes in the present work. However, we performed additional accuracy check using 1 billion (1B) photons for multiple scattering, OT = 1 and 0.25, $g = 1$, and $\cos(SZA) = 0.1$. For OT = 1, the 1B vs. 100M difference did not exceed 0.04% and 0.01% for intensity and degree of linear polarization, respectively. For OT = 0.25, the corresponding maximum errors are 0.03% (intensity) and 0.01% (degree of linear polarization). MYSTIC was used for this accuracy check.

The solar/view geometry for MYSTIC and MCSSA is defined at the location of the observer, which is TOA in our case. Given the definition at BOA, it is therefore necessary to translate the solar/view geometry from BOA to TOA to initiate the MC models. Table 2a-2b show the results of this geometry recalculation for the two SZAs in our work; figures are rounded off to 2 digits after the decimal point.

The third model is the discrete-ordinate RT code VLIDORT [24,25], which uses two approximate approaches to RT simulations in a spherical-shell atmosphere. In both approaches, single scattering is always simulated exactly in spherical geometry. In the first approach – the pseudospherical correction (VLPS) – calculations for second and higher orders of scattering are based on the assumption that solar beam attenuation is treated for a curved atmosphere, with propagation along the line-of-sight implemented in plane-parallel geometry. This approach is relatively easy to implement in plane-parallel RT code, but it suffers from lack of accuracy for larger VZA towards the horizon. In our paper, we illustrate accuracy levels for the VLPS approach and provide numerical results in Excel files uploaded to the journal website, but we do not embed VLPS numbers in the main text.

The second approach is based on a new multiple scatter spherical correction (VLSC) recently introduced to VLIDORT. As will be demonstrated, this approach delivers reasonable approximations to spherical-medium multiple scattering along the line of sight. The general idea behind this technique was briefly described in [14] and it is presented with some detail in the Appendix below. In addition, a full descrip-

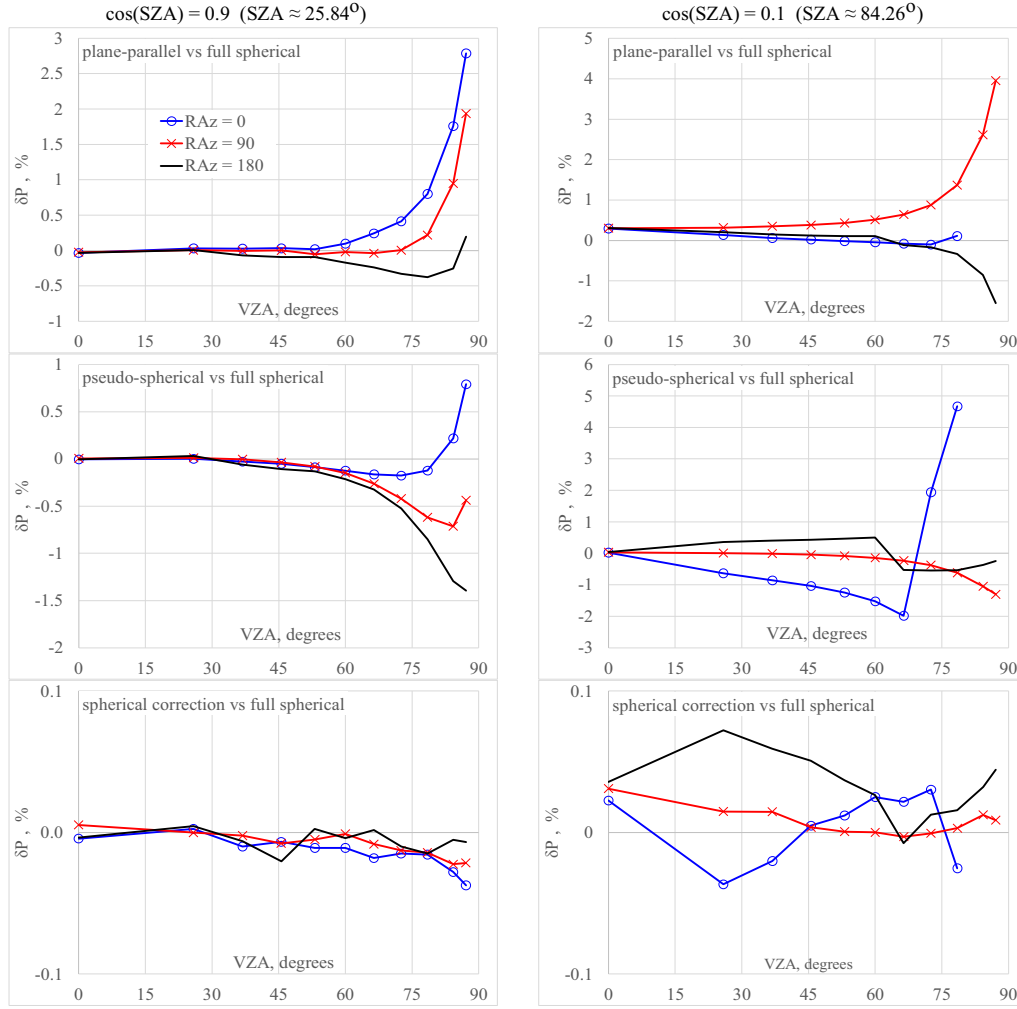


Fig. 6. Relative deviations for degree of linear polarization, P , as function of solar/view geometry for the atmosphere with an absorption profile, $g = 1$ in Eq. (1), and total $OT = 1$. Rows compare results with VLIDORT plane-parallel (top), pseudo-spherical (middle), and spherical correction (bottom) against full-spherical MC baselines. Refer to Table 2b for clarification regarding the two missing points, $\cos(VZA) = 0.1$ and 0.05 , for $\cos(SZA) = 0.1$ (right column) at $RAz = 0^\circ$ (blue line, circle marker).

tion of the correction will be described by its developer in a separate paper [26]. Unlike MC codes, VLIDORT always uses the solar/view geometry defined at BOA.

In order to ensure that our atmosphere has been set up properly and that the RT codes indeed achieve the desired accuracy level, we first reproduced the plane-parallel results from Mishchenko's paper [20] (not shown here). Then, we computed the total intensity I (both single and multiple scattering) and the degree of linear polarization P (also separately for single and multiple scattering), defined by

$$P = \sqrt{Q^2 + U^2} / I. \quad (3)$$

Percentage deviations δI and δP , are defined respectively as

$$\delta I = 100\% \cdot (I - I_0) / I_0, \quad \delta P = 100\% \cdot (P - P_0). \quad (4)$$

In Eq. (4), the subscript "0" stands for baseline results, which are generated by MYSTIC in our case. We chose MYSTIC because it is true-spherical and has been widely used in the RT community for a number of years. Positive deviations in Eq. (4) indicate that other RT code values exceed the baseline.

We present our results in three ways: figures, tables in the text and these same tables uploaded to the journal's website in digital format, and finally supplementary tables available only from the journal's website. The figures illustrate relative deviations of I and P for the plane-parallel, pseudo-spherical, and spherical correction modes in VLIDORT, from baseline full-spherical MYSTIC results. The figures should give the reader an overview of deviations using approximate methods. For the intensity, many similar figures may be found in the literature (see our review in [14]), but there are not so many for polarization.

Tables in the paper are limited to I and P only calculated using full-spherical MC codes MYSTIC and MCSSA (the two agree within 0.1% for all cases) and VLIDORT's multiple-scatter sphericity correction VLSC (for details on the sphericity correction choices in VLIDORT, see the Appendix). However, the supplementary material contains results for Stokes- Q and Stokes- U from the MYSTIC and VLIDORT models, in addition to I and P data. We preserve the original definitions of the U -signs in both codes, and note that

$$-U_{\text{Mishchenko}} = +U_{\text{VLIDORT}} = -U_{\text{MYSTIC}}. \quad (5)$$

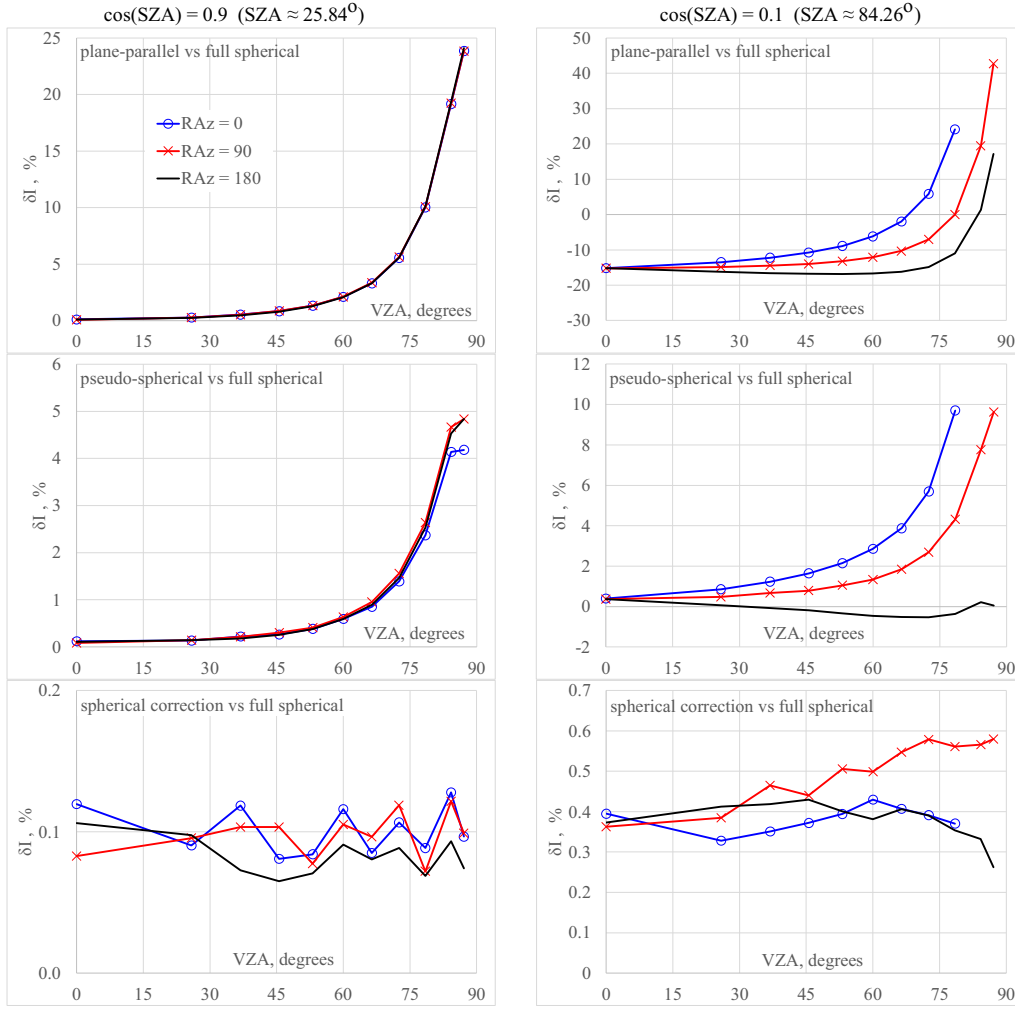


Fig. 7. Relative deviations for intensity, I , as function of solar/view geometry for the atmosphere with an absorption profile, $g = 1$ in Eq. (1), and total OT = 0.25. Rows compare results with VLIDORT plane-parallel (top), pseudo-spherical (middle), and spherical correction (bottom) against full-spherical MC baselines. Refer to Table 2b for clarification regarding the two missing points, $\cos(\text{VZA}) = 0.1$ and 0.05 , for $\cos(\text{SZA}) = 0.1$ (right column) at $\text{RAz} = 0^\circ$ (blue line, circle marker).

The difference in signs arises from definitions of system of coordinates for linear polarization. We refer our reader to Table 1 (page 34) in [9] for the Greek constants (phase matrix expansion coefficients) as they are used in VLIDORT; Table 1 in [20] for the alternative definition of these coefficients that causes differences in the U -component sign, Eq. (5); and to Eq. (88) in [5] for the connection between the two definitions. In the next section, all figures and tables with numerical results are referenced with the BOA solar/view geometry.

3. Graphical and numerical results

We illustrate the intensity and polarization deviations for two optical thickness values (0.25 and 1.0) and two atmospheres ($g = 0$ and $g = 1$) in eight separate figures, Fig. 1-8. Each figure contains 6 plots. Each plot shows deviations of the plane-parallel, pseudo-spherical VLPS, and spherically corrected VLSC computations from the baseline full-spherical MC MYSTIC. The deviations in each chart are plotted as a function of the view geometry: VZA on X-axis and three different lines with markers for three relative azimuths. Two columns correspond to $\text{SZA} \approx 25.84^\circ$ (left) and $\text{SZA} \approx 84.26^\circ$ (right). Figs. 1-4 pertain to the uniform atmosphere scenario with OT = 1 (Figs. 1-2) and OT=0.25 (Fig. 3-4). Figs. 5-8 show results for atmosphere with an absorption profile (OT = 1 in Figs. 5-6 and OT = 0.25 in Figs. 7-8). Intensity and degree of linear polarization deviations are plotted in odd- and even-numbered figures, respectively.

All figures show that the influence of the atmospheric curvature is high for the plane-parallel approximation (top rows in each figure). The errors for intensity at OT = 0.25 are higher compared to those for OT = 1. For the degree of linear polarization, the effect is the opposite: the optically thicker atmosphere leads to higher relative deviations. The monotonic error increase is caused by the monotonic increase of difference in OT when computed in the plane-parallel and spherical geometry, and the stronger influence of single scattering. Multiple scattering significantly complicates the picture. For the plane-parallel simulation at OT = 1 and $\text{SZA} \approx 25.84^\circ$ we used the original results from [20]: Table 3 for a uniform layer and Table 7 for a layer with a vertical profile. For other combinations of OTs and SZAs, we used VLIDORT operating in strict plane-parallel mode.

As noted already, the pseudo-spherical VLPS approximation (middle rows) takes solar beam attenuation for a curved atmosphere, with the single scattering radiation computed accurately in a spherical atmosphere, but computation of higher scattering orders ignor-

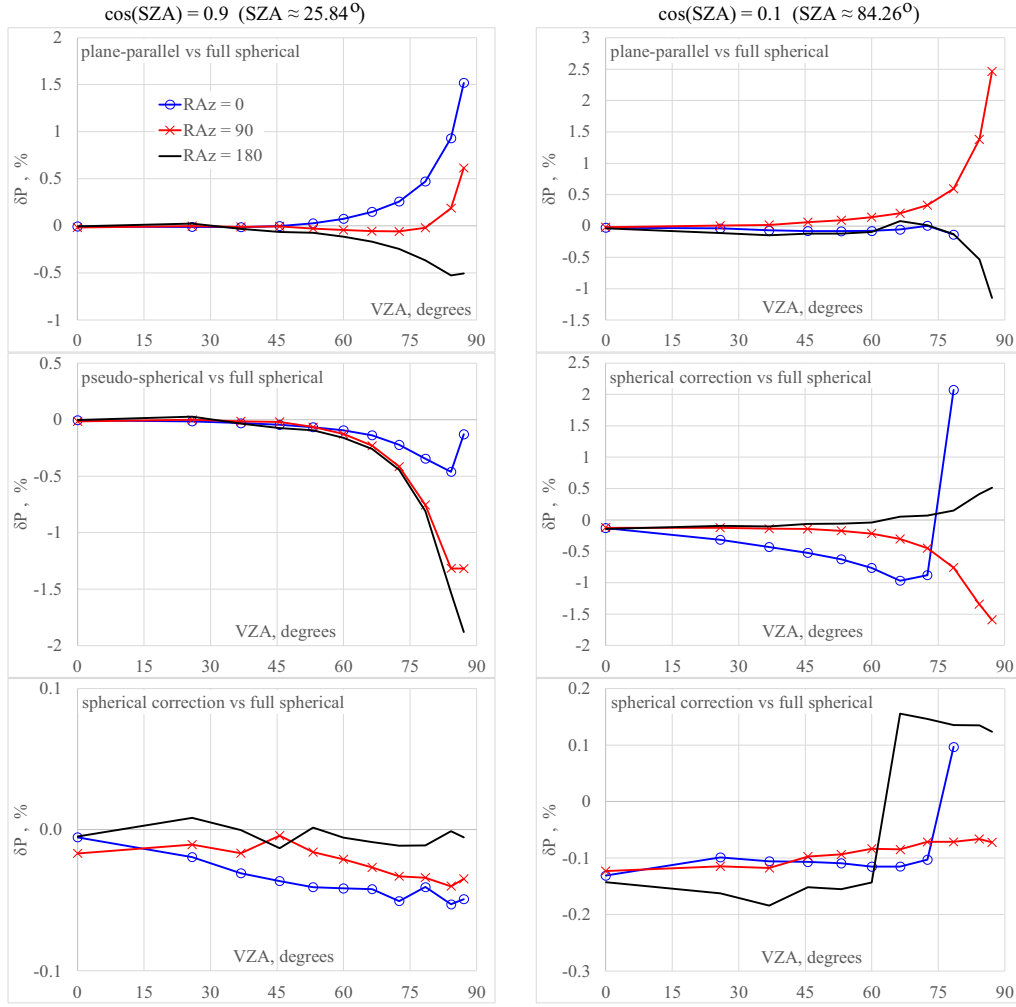


Fig. 8. Relative deviations for the degree of linear polarization, P , as function of solar/view geometry for the atmosphere with an absorption profile, $g = 1$ in Eq. (1), and total OT = 0.25. Rows compare results with VLIDORT plane-parallel (top), pseudo-spherical (middle), and spherical correction (bottom) against full-spherical MC baselines. Refer to Table 2b for clarification regarding the two missing points, $\cos(VZA) = 0.1$ and 0.05 , for $\cos(SZA) = 0.1$ (right column) at $RAz = 0^\circ$ (blue line, circle marker).

ing sphericity along the line of sight. The VLPS approach is useful for simulating light scattering close to nadir and has been widely used in satellite retrievals.

The VLIDORT multiple-scattering spherical correction VLSC (bottom rows) delivers the most accurate approximation for intensity and polarization. Deviations from MYSTIC are at the level of 0.1% - 0.5% in most cases. With such close agreement between VLSC and MC full-spherical results, the MC noise ($\sim 0.1\%$) is visible in all bottom charts of all Figs. 1-8.

To avoid excessive description, we refer the reader to the figures for the level of error in each case. Here we only note that there are a few unnatural-looking “jumps” appearing in the charts for the degree of linear polarization (e.g., Fig. 4: right column); these arise due to proximity to the neutral points in the radiation field, where the polarization is zero. All numerical results for Figs. 1-8 are available in digital form from the journal website; the Excel file names match the corresponding figure numbers.

Tables 3-10 contain new numerical results for intensity and degree of linear polarization as a function of the solar/view geometry and the scattering properties of the atmosphere. To support the development and validation of spherical RT codes, each table has two parts: (a) entries for multiple scattering fields (which includes single scattering); and (b) entries for the single scattering fields alone. The group of Tables 3-6 contains results for OT = 1; Tables 7-10 are for OT = 0.25. Table 3a-3b, Table 4a-4b, Table 7a-7b, and Table 8a-8b contain results for $SZA \approx 25.84^\circ$; Table 5a-5b, Table 6a-6b, Table 9a-9b, and Table 10a-10b – for $SZA \approx 84.86^\circ$. Finally, Table 3a-3b, Table 5a-5b, Table 7a-7b, and Table 9a-9b correspond to a single layer without absorption, $g = 0$, while Table 2a-Table 2b, Table 4a-4b, Table 6a-6b and Table 8a-8b are for $g = 1$ (see Eq. (1)).

In the tables, the columns from left to right indicate the following: RAz – relative azimuth (in degrees, with 0° corresponding to forward scattering, when the detector is “facing” the Sun) at BOA; $\cos(VZA)$ – cosine of the view zenith angle at BOA; MYSTIC: I and MYSTIC: P – the total intensity I and degree of linear polarization P computed with the Monte Carlo RT code MYSTIC; MCSSA: I and MCSSA: P – same but for RT code MCSSA; dI, % – relative deviation of intensities (in %) for MCSSA vs. MYSTIC (baseline); dP, % – deviation of degrees of linear polarization for MCSSA vs. MYSTIC (baseline), with the degree of linear polarization expressed in %; VLIDORT: I and VLIDORT: P – the total intensity I and degree of linear polarization P computed with VLIDORT operating in VLSC mode with the MS spherical correction; dI, % and dP, % – relative deviations (in %) for intensity and deviation for the degree of linear polarization (in %) for VLIDORT’s VLSC vs. MYSTIC (baseline).

We have also uploaded a set of tables for Stokes-Q and Stokes-U components for the spherical and plane-parallel computations listed in this paper. This data set is contained in eight auxiliary Excel files. Each filename indicates the SZA (truncated to the nearest integer value), the single (SS) or multiple (MS) scattering mode, and the atmospheric profile in terms of the number of layers: NL=001 and NL=100 correspond to a uniform layer and a layer with vertical profile. In each file, the reader will find two sheets for OT=1 and OT=0.25. All MS files contain plane-parallel results marked as ||. Since both MC codes, MYSTIC and MCSSA, agree within 0.1% for all cases and solar/view geometries, we have omitted Stokes-Q and Stokes-U results from MCSSA in the auxiliary Excel files.

For clarification, we summarize here the contents of just one file – all the others are organized in the same manner. The file `sza84_MS_NL100.xls` corresponds to the case with $SZA \approx 84.26^\circ$, or $\cos(SZA) = 0.1$, and vertical profile ($g = 1$ in Eq. (1)). The file contains two sheets for the two OTs named OT = 1 and OT = 0.25, respectively. In each sheet, columns from left to right are $\cos(SZA)$ - cosine of the solar zenith angle (constant along the sheet); RAZ - relative azimuth in degrees; II: I Q U P - three components of the Stokes vector and the degree of linear polarization for the plane-parallel atmosphere (not included in the SS-files); OMC: I Q U P - same for the full-spherical model; dI% - relative deviation in % of the total intensity for spherical vs plane-parallel case (the spherical result is assumed exact, the sign of error is preserved); dP% - absolute deviation of the degree of linear polarization (again, the spherical result is assumed exact and the sign of error is preserved); OVL: I Q U P - results for the multiple-scatter spherical correction in VLIDORT (VLSC); the last two columns dI% and dP% correspond to relative deviations of the intensity and degree of linear polarization between VLIDORT's VLSC results and the MYSTIC's full spherical baseline (the sign of the deviation is preserved). In the bottom, the reader will find maximum and average deviations for I and P - this time the sign of the deviation is ignored. For an overview, these maximum and average errors are gathered in Table 11 (a-c) in the Conclusion.

4. Conclusion

In this paper we have extended numerical benchmarks for the RT scenario defined by Michael Mishchenko [20] to include curvature of the Earth's atmosphere. For the independent reproducibility of our results, we have defined all input parameters in this paper as well as in uploaded supplemental files. Numerical results are available in the text of the paper and from the website in digital form. Separate results are given for single and multiple (including single) scattering, two OTs = 1 and 0.25, a uniform atmosphere and one with an absorption profile. These intensity and polarization results support the development and validation of a spherical polarized (vector) RT code.

The effect of sphericity on the reflected intensity has been discussed in many publications. Differences between the plane-parallel and spherical model results increase as the zenith angle (solar and/or view) tends towards the horizon. Similar effects appertain to polarization, but its azimuthal dependence is both strong and non-monotonic. The presence of skylight neutral points complicates the picture even further. However, percentile deviations for polarization are much smaller, up to 5% in our case, while those for intensity can exceed above 90% (even if we skip the geometries where the line of sight misses BOA). Table 11a summarizes maximum (and average) errors for the spherical vs. plane-parallel case.

Results reported in this paper were obtained using RT codes MYSTIC and MCSSA (Monte Carlo models, full-spherical) and VLIDORT (discrete ordinate model operating in two modes: pseudo-spherical VLPS and multiple-scatter spherical correction VLSC). Although the VLPS option is more convenient and often (but not always) gives results closer to full-spherical values as compared to the strict plane-parallel situation, the accuracy may not be sufficient as Table 11b shows.

The multiple-scatter spherical correction in VLIDORT, VLSC - Table 11c - yields sufficiently accurate results while maintaining the computational efficiency close to that for the VLSC mode. The numbers for intensity in Table 11c agree well with those we reported earlier [14]: Table 7 but they are slightly higher because in the vector case, errors in simulation of the Q and U components have contributed.

Comparing results from the constant OT atmospheric scenario with those obtained using the exponential-profile scenarios as defined in Mishchenko's plane-parallel test, we found that deviations from MC spherical results are similar in both cases.

To keep our results concise and easy to reproduce, we have not considered several important RT aspects in this paper. These include a reflecting surface, transmitted radiation, stratospheric aerosol and/or cloud layers (e.g., cirrus), and most importantly, a higher ratio of the TOA to BOA radii to highlight the effect of planet curvature (e.g., Titan). We plan to cover some of these topics in our next papers. Our efforts have continued the work by Michael Mishchenko [20] on the publication of accurate benchmark results for RT numerical simulations.

Declaration of Competing Interest

None

Acknowledgements

The work of Alexei Lyapustin and Sergey Korkin was partially supported by the NASA DSCOVR EPIC program (manager Dr. R. Eckman) and NNH19ZDA001N-ESROGSS program (manager Dr. T. Lee). Pengwang Zhai is partially supported by NASA Grant: 80NSSC20M0227; he is also thankful to Charles Adams for sharing Monte Carlo RT code for spherical geometry.

Supplementary materials

Supplementary material associated with this article can be found, in the online version, at doi:10.1016/j.jqsrt.2022.108194.

Appendix A. VLSC - Multiple-scattering Sphericity Corrections in VLIDORT

We wish to use VLIDORT to calculate the upwelling Stokes-vector field at the top of the spherical atmosphere (TOA), given the 3-angle input geometry specified at the bottom of the atmosphere (BOA). These angles are: solar zenith angle (SZA; $\cos(SZA) = \mu_0$), view zenith angle (VZA; $\cos(VZA) = \mu$; $\mu = \mu_- < 0$ for upwelling radiation) and relative azimuth (RAZ; φ). VZA and RAZ determine the line-of-sight

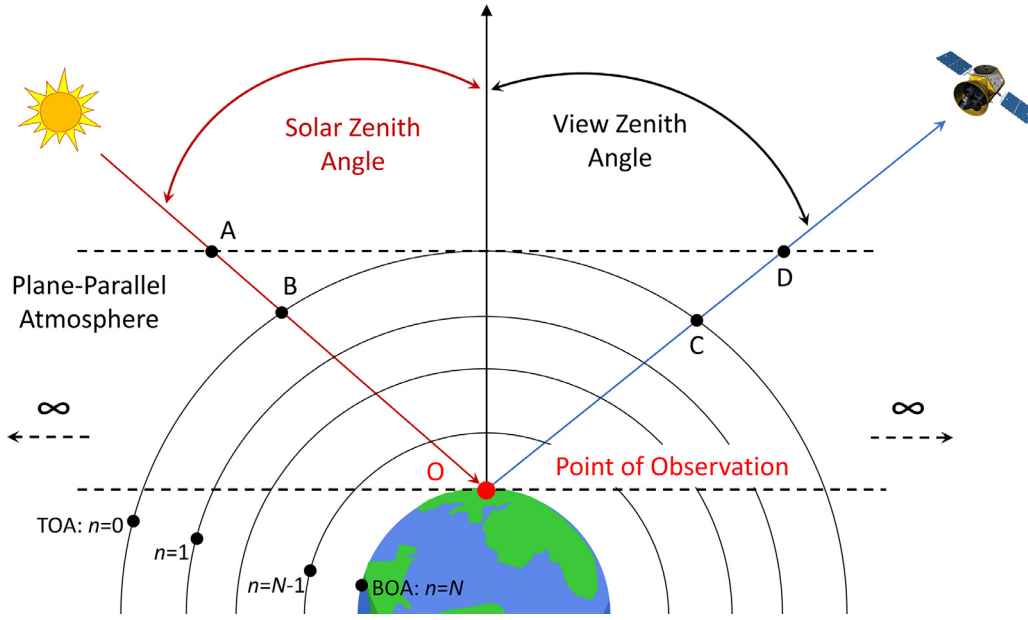


Figure A. Plane-parallel vs spherical geometry.

(LOS). In this situation, a *standard* call to VLIDORT will perform a plane-parallel multiple scatter calculation based solely on the BOA input geometry; only the solar-beam attenuation (see Fig. A, segments AO vs BO) and single scattering terms are treated for a curved medium neglecting refraction (this is the so-called pseudo-spherical approximation – VLPS). In other words, all layer-by-layer multiple scatter (MS) source terms (MSST, i.e. second and higher orders of scattering) along the LOS path depend only on the BOA geometry – there are no means to account for changes in the LOS-path geometry when following the path from BOA to TOA (see Fig. A, segments OC vs OD).

The new “sphericity correction” in VLIDORT (VLSC) aims to provide more accurate determination of these MSSTs by application of a simple strategy for allowing MS geometries to change along LOS paths. We now summarize this strategy.

Step A: The single-scatter Stokes field is treated exactly in spherical geometry. This calculation allows for changing geometry along the LOS from BOA to TOA, and accurate solar-beam ray-tracing is carried out at every point along this path. To ensure smooth changes in the solar view geometry at every point $n = 0, 1, \dots, N$, the atmosphere is divided into a number of shell layers (100 in this paper) – see Fig. A. The multi-layer single scattering evaluation is essentially analytical, and its computation time is negligible compared with the overall runtime. For a reflecting surface, the “direct-bounce” contribution from the reflected solar beam at BOA to any point along the LOS in the spherical atmosphere is also computed precisely.

Step B: VLIDORT computes multiple scattering (MS) at discrete ordinates (Gauss-Legendre quadrature nodes) using the plane-parallel approximation. In each layer, *homogeneous* radiative transfer solutions at these nodes are determined with eigenproblem analysis. In VLIDORT, the complete discrete ordinate radiation field \mathbb{X} is determined through inversion of a large sparse banded linear algebra system $\mathbb{A}\mathbb{X} = \mathbb{B}$ resulting from imposition of boundary conditions at TOA and BOA and continuity of RT solutions at intermediate layer boundaries. The formal solution is $\mathbb{X} = \mathbb{A}^{-1}\mathbb{B}$. Vector \mathbb{B} is a composite of particular integral RT solutions depending on the solar source terms, and matrix \mathbb{A} contains entries that are constructed only from the discrete ordinate eigensolutions. Along with calculations for eigensolutions, it is the (numerical) determination of the inverse matrix \mathbb{A}^{-1} that is the most time-consuming element in the VLIDORT call. In this regard, we note that eigenvectors and eigenvalues depend only on optical properties of the atmosphere, not on the TOA and BOA boundary conditions, and not on any source terms. For details of this summary, see the VLIDORT literature (e.g. Spurr, [24]).

The new multiple sphericity correction in VLIDORT requires several particular-integral solutions with different solar-view geometries, and for this we utilize the VLIDORT facility for handling multiple solar source terms within a single call to the model. As noted above, eigenproblem solutions and inversion of the boundary problem matrix need to be determined just once, no matter how many solar beams are present; indeed, calling VLIDORT with 2 solar beams does not mean that the run time will double.

Step C: The source function integration technique (along the LOS) is used to compute the final Stokes vector for a given user-defined direction (VZA, RAZ) [17]. We start with the complete solution (with solar source terms) at the discrete ordinates (Gauss-Legendre nodes), at any point in the atmosphere. This solution is then substituted back into the multiple-scatter element of the RTE in order to simulate scattering into the LOS direction at this same point. The accumulation of radiation at points along the LOS, from BOA to TOA, yields the TOA signal. Key equations for this important step are given below for upwelling radiation ($\mu_- < 0$), using a scalar treatment (no polarization) for ease of explanation.

We write down the LOS upwelling radiation at the upper boundary of the layer n as follows:

$$I(\tau_{n-1}, \mu_-, \varphi) = I(\tau_n, \mu_-, \varphi)T_n + I_1(\Delta\tau, \mu_-, \varphi) - \frac{1}{\mu_-} \int_{\Delta\tau} J(t, \mu_-, \varphi) \exp\left(\frac{t}{\mu_-}\right) dt \quad (\text{A1})$$

In Eq. (A1), $\Delta\tau = \tau_n - \tau_{n-1}$ is the optical thickness of layer n , $I(\tau_n, \mu_-, \varphi)$ is the upwelling full scattering radiance at the bottom of the layer, $T_n = \exp(\Delta\tau/\mu_-)$ is the LOS path transmittance through the layer, and $I_1(\Delta\tau, \mu_-, \varphi)$ is the single-scatter layer source term.

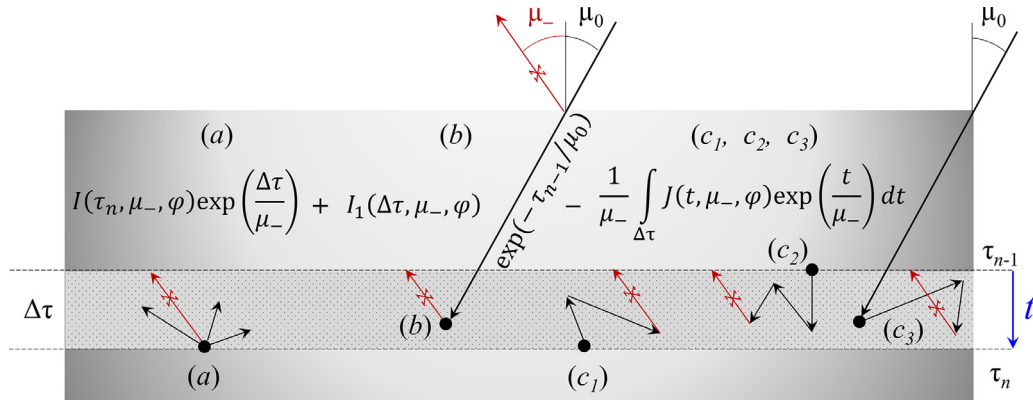


Figure B. Illustration for Eq. (A1), upwelling radiation (X-marked red): (a) direct contribution of scattered radiation from the bottom layer; (b) single scatter contribution from the element layer $\Delta\tau$; (c1) and (c2) “re-scattering” of diffuse radiation coming respectively from layers below and above the given layer $\Delta\tau$; (c3) multiple scattering of direct solar beam within the given layer $\Delta\tau$ (note, element (c3) is missing in [32]: Fig. 4 by mistake). Note, $\mu_- = \cos(\text{VZA})$ is negative, and $\mu_0 = \cos(\text{SZA})$ is positive. The dark-red arrow (X-marked for black-and-white printing) is the user-defined line-of-sight.

The remaining entry in this equation is

$$M = -\frac{1}{\mu_-} \int_{\Delta\tau} J(t, \mu_-, \varphi) \exp\left(\frac{t}{\mu_-}\right) dt \quad (\text{A2})$$

which is the multiple scatter (MSST) layer source terms. The latter depends on the phase function $p(\mu, \mu', \varphi, \varphi')$ and diffuse radiance $I(\tau, \mu', \varphi')$ through the source term field

$$J(\tau, \mu, \varphi) = \frac{\omega_0}{4\pi} \int_0^1 \int_{-1}^1 p(\mu, \mu', \varphi, \varphi') I(\tau, \mu', \varphi') d\mu' d\varphi'. \quad (\text{A3})$$

As indicated in Fig. B, the multiple scatter layer source term is “connected” to the neighboring layers by “re-scattering” radiation coming from them. It is common practice in RT to integrate over azimuth using Fourier decomposition and over polar directions using discrete ordinate nodes. Since the complete RT solution anywhere in the atmosphere at Gauss nodes has been found (see **Step B** above), it follows that single and multiple scatter source terms can be computed numerically.

Step D: Based on the analysis in Step C, VLIDORT will calculate a set of multiple scatter source term (MSST) functions, Eq. (A2) for the solar-view geometry defined at BOA for each layer of the atmosphere. In addition, for a reflecting surface, VLIDORT will also calculate the diffusely-reflected surface term, S_b , which is computed from knowledge of the downwelling discrete ordinate solution at BOA (**Step B**), the surface boundary condition (Lambertian or BRDF), and the LOS geometry at BOA. This is the standard VLPS VLIDORT solution for a single solar-beam geometry at BOA.

Step E: Next, the multiple scatter layer source terms (MSSTs) are computed for additional solar/view geometries at specific points along the LOS. These geometries are determined through simple spherical geometry calculations. Depending on the desired accuracy and runtime tolerance, the user may choose to compute the MSST sets for solar geometries at 2 points (BOA & TOA – this is the minimum), at 3 points (BOA, TOA, and at a single LOS location in between), or at multiple LOS positions at all intervening layer boundaries. In order to follow the smooth changes in geometrical configurations along the line of sight, these sets of MSSTs at different 2-, 3-, or multiple points are linearly interpolated in each layer (with cosine of the VZA). The final set of interpolated MSSTs is then used to accumulate signal along the LOS.

Here, we illustrate this strategy with equations showing how these interpolated MSSTs are used in the final source function integration.

For the Stokes vector (bold symbols), the LOS upwelling Stokes vector at the top of layer is identical to that in Eq. (A1)

$$\mathbf{I}_{n-1}^\uparrow = T_n \mathbf{I}_n^\uparrow + \mathbf{S}_n^\uparrow + \tilde{\mathbf{M}}_n^\uparrow \quad (\text{A4})$$

In Eq. (A4), \mathbf{I}_n^\uparrow is the Stokes vector at the bottom of the layer, T_n is the LOS path transmittance through the layer (see first term in the right-hand side in Eq. (A1)), \mathbf{S}_n^\uparrow is the single scatter layer source term (2nd term in the right-hand side in Eq. (A1)) and $\tilde{\mathbf{M}}_n^\uparrow$ is the interpolated multiple scatter layer source terms (MSST, see 3rd term in Eq. (A1) and Eq. (A2) and Eq. (A3)) as outlined above. We will explain the meaning of the “~” sign at $\tilde{\mathbf{M}}_n^\uparrow$ later, at Eq. (A10).

For a reflecting surface at BOA, the upwelling reflected Stokes vector \mathbf{I}_{Surf} is the sum of two parts – the “direct-bounce” solar beam reflection \mathbf{I}_{DB} and the diffusely-reflected term \mathbf{I}_{DR}

$$\mathbf{I}_{Surf} = \mathbf{I}_{DB} + \mathbf{I}_{DR} \quad (\text{A5})$$

These two quantities are immediately available from VLIDORT.

In order to obtain the upwelling field at TOA, we apply Eq. (A4) recursively, starting from \mathbf{I}_{Surf} at BOA, and ending with the TOA field \mathbf{I}_0^\uparrow , as follows:

$$\mathbf{I}_{TOA}^\uparrow = \mathbf{I}_0^\uparrow = \mathbf{I}_{TOA, SS}^\uparrow + \mathbf{I}_{TOA, MS}^\uparrow \quad (\text{A6})$$

$$\mathbf{I}_{TOA, SS}^{\uparrow} = C_N \mathbf{I}_{DB} + \sum_{n=1}^N C_{n-1} \mathbf{S}_n^{\uparrow} \quad (\text{A7})$$

$$\mathbf{I}_{TOA, MS}^{\uparrow} = C_N \mathbf{I}_{DR} + \sum_{n=1}^N C_{n-1} \mathbf{M}_n^{\uparrow} \quad (\text{A8})$$

$$C_n = \prod_{p=1}^n T_p; \quad C_0 = 1. \quad (\text{A9})$$

Here, we are using the cumulative transmittances $\{C_n\}$, and N is the total number of layers in the atmosphere. The single scatter contribution $\mathbf{I}_{TOA, SS}^{\uparrow}$ is already known from the spherically accurate single-scatter calculation done first in VLIDORT before the MS computation.

According to Step D above, VLIDORT running in VLSC mode will return a set of MS source terms $\{\mathbf{M}_{n, g(N)}^{\uparrow}\}$, $n = 1, 2, \dots, N$, appropriate to the BOA solar/view geometry. This 3-angle geometrical input is indicated with a second suffix $g(n)$; here, $g(N)$ indicates the solar/view geometry at the lower boundary of layer N , which is BOA. Using the BOA geometry set $\{\mathbf{M}_{n, g(N)}^{\uparrow}\}$ for $\{\mathbf{M}_n^{\uparrow}\}$ in Eq. (A8) will result in increasing errors as the LOS path geometrical configuration moves further away from its starting value at BOA.

To correct for this, we can instruct VLIDORT in VLSC mode to make a second MS calculation for the geometrical calculation $g(0)$ at TOA at the end of the LOS path. This gives us a second set of MS source terms $\{\mathbf{M}_{n, g(0)}^{\uparrow}\}$, $n = 1, 2, \dots, N$. The 2-point sphericity correction works as follows. For each layer along the LOS we interpolate between these two BOA and TOA MSSTs sets, linearly with the cosine of the LOS zenith angle (the “~” accent indicates interpolated values and μ_0 in Eq. (A10) is the cosine of the LOS at BOA, $n = 0$, not the cosine of the solar zenith):

$$\tilde{\mathbf{M}}_n^{\uparrow} = \frac{1}{(\mu_N - \mu_0)} \left((\mu_N - \tilde{\mu}_n) \mathbf{M}_{n, g(0)}^{\uparrow} + (\tilde{\mu}_n - \mu_0) \mathbf{M}_{n, g(N)}^{\uparrow} \right), \quad n = 1, \dots, N. \quad (\text{A10})$$

In layer n , Eq. (A10), we have assumed that the LOS viewing zenith angle cosine $\tilde{\mu}_n$ is the mid-point (average) value in the layer: $\tilde{\mu}_n = (\mu_n + \mu_{n-1})/2$, where $\{\mu_n\}$, $n = 0, 1, \dots, N$ are the view-path cosines at layer boundaries from TOA to BOA. It is this interpolated set $\{\tilde{\mathbf{M}}_n^{\uparrow}\}$ that we now use in Eq. (A4) to generate the required MS field at TOA. Note that the surface diffuse-reflection contribution \mathbf{I}_{DR} is determined only with the BOA geometry configuration $g(N)$.

VLIDORT also has a 3-point spherical correction. Here, MSST calculations in VLIDORT are done three times for three different geometrical inputs – at BOA geometry $g(N)$, TOA geometry $g(0)$, and at a suitably chosen intermediate geometry $g(P)$ for a point P along the LOS. Interpolation is still done linearly with LOS view-zenith angle cosines, only now there are two regimes to consider: either the layer average value $\tilde{\mu}_n \in [\mu_N, \mu_P]$ in the lower section of the LOS, or $\tilde{\mu}_n \in [\mu_P, \mu_0]$ in the upper section. Using the 3-point interpolation requires a call to VLIDORT with 3 input geometries, and although results are more accurate than those from the 2-point correction, the computation is a little slower.

The third and most accurate option for VLSC is to operate with a multi-point spherical correction. For this, MSST sets $\{\mathbf{M}_{n, g(p)}^{\uparrow}\}$, $n = 1, 2, \dots, N$, $p = 0, 1, 2, \dots, N$ are calculated for a whole series of geometrical configurations at all intermediate layer boundaries $p = 0, 1, 2, \dots, N$ along the line of sight, and in each layer we use the average values from adjacent sets

$$\tilde{\mathbf{M}}_n^{\uparrow} = \frac{1}{2} \left(\mathbf{M}_{n, g(n)}^{\uparrow} + \mathbf{M}_{n, g(n-1)}^{\uparrow} \right), \quad n = 1, 2, \dots, N. \quad (\text{A11})$$

With many more MSST sets to determine, this option is obviously more computationally expensive.

From a practical standpoint when using these corrections, there are two stages. The first stage is the VLIDORT call, for which the outputs are $\mathbf{I}_{DR, g}$ (for the diffuse surface reflectance) and $\{\mathbf{M}_{n, g}^{\uparrow}\}$, $n = 1, \dots, N$ for the multiple scatter layer source terms at each geometrical configuration g (2 values of g for the 2-point, 3 values of g for the 3-point, and $N+1$ values for the multi-point correction). The second stage is to perform the requisite interpolation of layer MSSTs according to the choice of interpolation scheme, Eqs. (A10) or (A11), and then apply the recursion relations in Eq. (A4) to deliver the TOA Stokes vector. A dedicated software module has been written to execute this second stage, which takes place after VLIDORT is called.

At present, the VLSC interpolations, Eqs. (A10)-(A11), and recursions, Eqs. (A5)-(A9), are done separately outside VLIDORT after the Fourier-azimuth series convergence. This ensures that all MSSTs are calculated to the level of accuracy specified as one of the inputs to VLIDORT. However, it is possible to calculate the MSSTs in Fourier space alone, then carry out the VLSC interpolations for Fourier components of the TOA Stokes vector, and finally completing the calculation by performing azimuth convergence using RAz values at TOA. This alternative approach would require significant modification of the existing VLIDORT core solver; we plan to consider this alternative in a separate publication.

Finally, we note that the sphericity correction has also been given a full linearization capability, that is, the simultaneous generation of analytically-derived weighting functions (Jacobians) with respect to any surface or atmosphere property. Note also that this sphericity correction will work for the accurate calculation of downwelling radiation fields at BOA; the formulation is very similar to the above, but without the surface terms.

References

- [1] Adams CN, Kattawar GW. Radiative transfer in spherical shell atmospheres. I. Rayleigh scattering. *Icarus* 1978;35:139–51.
- [2] Bodhaine B, Wood NB, Dutton EG, Slusser JG. On Rayleigh optical depth calculations. *J Atmos Ocean Tech* 1999;16:1854–61.
- [3] Chandrasekhar S. Radiative Transfer. London: Oxford University Press; 1950.
- [4] Christensen ER. Computer simulation of photons in spherical media for density gauges. *Comput Phys Commun* 1974;7:192–9.
- [5] de Rooij WA, van der Stap CCAH. Expansion of Mie scattering matrices in generalized spherical functions. *Astron Astrophys* 1984;131:237–48.

- [6] Emde C, Mayer B. Simulation of solar radiation during a total eclipse: a challenge for radiative transfer. *Atmos Chem Phys* 2007;7:2259–70.
- [7] Emde C, Buras R, Mayer B, Blumthaler M. The impact of aerosols on polarized sky radiance: model development, validation, and applications. *Atmos Chem Phys* 2010;10:383–96.
- [8] Emde C, Buras-Schnell R, Kylling A, Mayer B, Gasteiger J, Hamann U, Kylling J, Richter B, Pause C, Dowling T, Bugliaro L. The libRadtran software package for radiative transfer calculations (version 2.0.1). *Geosci Model Dev* 2016;9:1647–72. Note: v.2.0.4 is the latest version.
- [9] Garcia RDM. Radiative transfer with polarization in a multi-layer medium subject to Fresnel boundary and interface conditions. *J Quant Spectrosc Radiat Transfer* 2013;115:28–45.
- [10] Garcia RDM. Accurate spherical harmonics solutions for neutron transport problems in multi-region spherical geometry. *J Comput Phys* 2021;424:109856.
- [11] Hummer DG, Kunasz CV, Kunasz PB. Numerical evaluation of the formal solution of radiative transfer problems in spherical geometries. *Comput Phys Commun* 1973;6:38–57.
- [12] Karp AH. Recent advances in the spherical harmonics method. *Int J Eng Sci* 1998;36:1551–68.
- [13] Korkin S, Lyapustin A, Sinyuk A, Holben B, Kokhanovsky A. Vector radiative transfer code SORD: performance analysis and quick start guide. *J Quant Spectrosc Radiat Transfer* 2017;200:295–310.
- [14] Korkin S, Eun-Su Y, Spurr R, Emde C, Krotkov N, Vasilkov A, et al. Revised and extended benchmark results for Rayleigh scattering of sunlight in spherical atmospheres. *J Quant Spectrosc Radiat Transfer* 2020;254:107181.
- [15] Lahdour M, El Bardouni T, El Hajjaji O, Chakir E, Ziani H, Al Zain J, et al. OpenNTP: implementation of the SN method in cartesian 2D geometry and the CP method in cylindrical and spherical 1D geometry. *Comput Phys Commun* 2021;261:107812.
- [16] Lary DJ, Balluch M. Solar heating rates: the importance of spherical geometry. *J Atmospheric Sci* 1993;50(24):3983–93.
- [17] Lenoble J, editor. Radiative transfer in scattering and absorbing atmospheres: standard computational procedures. Hampton VA: A. Deepak Publishing; 1985.
- [18] Mayer B, Kylling A. Technical note: The libRadtran software package for radiative transfer calculations - description and examples of use. *Atmos Chem Phys* 2005;5:1855–77.
- [19] Mayer B. Radiative transfer in the cloudy atmosphere. *Eur Phys J Conf* 2009;1:75–99.
- [20] Mishchenko MI. The fast invariant imbedding method for polarized light: computational aspects and numerical results for Rayleigh scattering. *J Quant Spectrosc Radiat Transfer* 1990;43:163–71.
- [21] Mishchenko MI, Lacis AA, Travis LD. Errors induced by the neglect of polarization in radiance calculations for Rayleigh-scattering atmospheres. *J Quant Spectrosc Radiat Transfer* 1994;51:491–510.
- [22] Rozanov AV, Rozanov VV, Burrows JP. Modeling of inelastically scattered radiation: rotational Raman scattering in the spherical Earth's atmosphere. *J Quant Spectrosc Radiat Transfer* 2021;268:107611.
- [23] Spagna GF, Leung CM. DUSTCD: A radiative transport code for spherically symmetric dust clouds. *Comput Phys Commun* 1983;28:337–53.
- [24] Spurr RJD. VLIDORT: A linearized pseudo-spherical vector discrete ordinate radiative transfer code for forward model and retrieval studies in multilayer multiple scattering media. *J Quant Spectrosc Radiat Transfer* 2006;102:316–42.
- [25] Spurr R, Christi M. The LIDORT and VLIDORT linearized scalar and vector discrete ordinate radiative transfer models: updates in the last 10 years. In: Kokhanovsky A, editor. Springer series in light scattering; 2019. p. 1–62.
- [26] Spurr R, Natraj V, Colosimo SF, Stutz J, Christi M, Korkin S. VLIDORT-QS: A quasi-spherical vector radiative transfer model. *J Quant Spectrosc Radiat Transfer* 2022 in preparation.
- [27] van de Hulst. Radiative transfer in a spherical dust cloud. I: exact results for isotropic scattering. *Astron. Astrophys* 1987;173:115–23.
- [28] van de Hulst. Radiative transfer in a spherical dust cloud. II. Asymptotic form of the reflection function for isotropic scattering. *Astron. Astrophys* 1988;207:182–93.
- [29] Zawada D, Franssens G, Loughman R, Mikkonen A, Rozanov A, Emde C, et al. Systematic comparison of vectorial spherical radiative transfer models in limb scattering geometry. *Atmos Meas Tech* 2021;14(5):3953–72.
- [30] Zhai P-W, Hu Y. An improved pseudo spherical shell algorithm for vector radiative transfer. *J Quant Spectrosc Radiat Transfer* 2022;282:108132.
- [31] Emde C, Barlakas V, Cornet C, Evans F, Korkin S, Ota Y, et al. IPRT polarized radiative transfer model intercomparison project – Phase A. *J Quant Spectrosc Radiat Transfer* 2015;164:8–36. doi:10.1016/j.jqsrt.2015.05.007.
- [32] Korkin S, Sayer A, Ibrahim A, Lyapustin A. A practical guide to writing a radiative transfer code. *Comput Phys Commun* 2022;271:108198. doi:10.1016/j.cpc.2021.108198.